

HIGH SPATIAL RESOLUTION ISOTOPIC CO AND CS OBSERVATIONS OF M17 SW: THE CLUMPY STRUCTURE OF THE MOLECULAR CLOUD CORE

J. STUTZKI¹ AND R. GÜSTEN²

Received 1989 September 8; accepted 1989 December 20

ABSTRACT

We present high-angular resolution maps of the M17 SW cloud core in the $\text{C}^{18}\text{O } J = 2 \rightarrow 1$ (13" FWHM beam) and $\text{C}^{34}\text{S } J = 2 \rightarrow 1$ (27" FWHM), $3 \rightarrow 2$ (17" FWHM) lines obtained with the IRAM 30 m telescope. These maps directly reveal the clumpy structure of the entire cloud core down to linear scales of 0.14 pc (13") and below. Individual clumps have line widths as small as 0.5 km s^{-1} , compared to a line width of $3\text{--}5 \text{ km s}^{-1}$ observed with lower angular resolution in the same lines. The $\text{C}^{18}\text{O } 2 \rightarrow 1$ line reaches a peak brightness temperature of 24 K in the 13" beam and is probably slightly optically thick in several locations.

Spectra in the more abundant CO isotopes obtained toward several selected positions show strong self-absorption notches and peak brightness temperatures in between these notches of about 100 K. The main isotope emission comes from only a small fraction of the total material with extreme physical conditions not at all characteristic of the bulk of the cloud.

The $\text{C}^{18}\text{O } J = 2 \rightarrow 1$ emission traces the same high-density material visible in the C^{34}S lines. A decomposition of the $\text{C}^{18}\text{O } 2 \rightarrow 1$ emission into Gaussian-shaped clumps identifies ≈ 180 clumps with masses ranging from a few to a few thousand M_{\odot} and densities between $10^5\text{--}10^6 \text{ cm}^{-3}$. The ensemble of all clumps fills about 30% of the total volume; the volume filling factor for clumps with densities greater than 10^5 cm^{-3} is only 13%. We estimate a clump/interclump density contrast of at least 23. The mass spectrum of the clumps closely follows a power law, $dN/dM = M^{-\alpha}$, with $\alpha = 1.7 \pm 0.15$.

Subject headings: interstellar: abundances — interstellar: molecules — nebulae: individual (M17)

1. INTRODUCTION

There is increasing evidence that clumpiness is a general property of molecular clouds and plays a key role in understanding the fragmentation of cloud complexes into subclouds finally small enough to form individual stars. Until recently, the observational evidence for clumpiness has been only indirect. Whereas ^{12}CO observations in the low- J millimeter lines are usually interpreted to show optically thick, thermalized emission from smoothly distributed, rather low density (several 10^3 cm^{-3}) gas, observations of molecules tracing higher density regions generally indicate that the emission does not come from the fact that the increase of line width with HCN, H_2CO , and CS ($\approx 10^5\text{--}10^6 \text{ cm}^{-3}$; Snell *et al.* 1984; Evans *et al.* 1987; Mundy *et al.* 1986, 1987) showed that the derived virial masses are in conflict with a homogeneous cloud at the density derived from a multilevel excitation analysis. The only way out is to assume a small volume filling factor of the emitting gas, implying that the sources have substantial structures on scales smaller than the beam size.

For NH_3 (density around several 10^4 cm^{-3}), the observed main beam brightness temperatures are generally only 10%–20% of the temperatures expected for thermalized emission from a homogeneous cloud and, due to the presence of the nuclear hyperfine transitions, the excitation conditions are constrained well enough that this discrepancy cannot be explained by subthermal or optically thin emission (e.g., Ho and Townes 1983). This discrepancy thus indicates beam filling factors of order 0.1 for most warm clouds (e.g., Ho and Townes 1983). Similarly, the presence of hyperfine intensity anomalies

in the NH_3 inversion emission from at least 50% of the cloud cores observed in ammonia (Stutzki *et al.* 1984) implies that the clouds consist of many clumps, with the line width of individual clumps being much smaller ($\leq 0.3 \text{ km s}^{-1}$) than the observed width of the ammonia lines ($\sim 2 \text{ km s}^{-1}$) (Matsakis *et al.* 1977; Stutzki and Winnewisser 1985).

Independent, but also indirect, evidence for clumpiness comes from the fact that the increase of line width with optical depth in comparing the emission from different isotopes (e.g., ^{12}CO , ^{13}CO , and C^{18}O) is much smaller than expected on the basis of a microturbulent, homogeneous cloud model. Martin, Sanders, and Hills (1984) showed in a case study of M17 that the assumption of a clumpy cloud structure, both in the spatial distribution and in velocities ("macroturbulence"), can explain the observations much better. Their model has about seven fragments along each line of sight. They estimate a volume filling factor of the clumps ≈ 0.1 .

A clumpy cloud structure with a high-density contrast between clump and interclump medium also naturally explains the spatial correlation between the atomic fine-structure emission from C I or C II, warm molecular CO, and bulk CO emission observed across the M17 SW interface (Keene *et al.* 1985; Harris *et al.* 1987; Genzel *et al.* 1988; Stutzki *et al.* 1988). Due to clumpiness of the cloud material, UV radiation can penetrate further into the cloud, dissociating the molecules and ionize the atoms, than if the cloud were homogeneous. In addition, the very extended C II emission detected in both M17 (Stutzki *et al.* 1988) and Orion (Stacey *et al.* 1989) implies the presence of UV photons in the range 912–2000 Å throughout the clouds, i.e., over length scales at least an order of magnitude larger than the UV absorption length estimated from the average cloud density. Recent theoretical work on radiative

¹ Max-Planck-Institut für Physik und Astrophysik, Institut für Extraterrestrische Physik.

² Max-Planck-Institut für Radioastronomie.

transfer in a clumpy environment (Boissé 1989) supports the simple modeling (Stutzki *et al.* 1988) of the much slower UV attenuation in the clumpy cloud core.

Recent observations of high-density tracing molecular lines in a few sources (CS $J = 7 \rightarrow 6$ in NGC 2024; Moore *et al.* 1989; H₂CO in S140: Evans, Kutner, and Mundy 1987), have shown several individual clumps, thus confirming the indirect evidence for clumpiness discussed above. Few direct estimates of molecular cloud fragmentation using CO or isotopic CO lines, and thus tracing the bulk of the molecular material, have been reported in the literature. C¹⁸O $J = 1 \rightarrow 0$ emission from the Orion core shows several clumps (Wilson *et al.* 1986). The sensitive ¹³CO surveys of cool giant molecular clouds (lacking associated massive star formation) obtained by Pérault, Falgarone, and Puget (1985) show direct evidence for the clumpy nature of these clouds. This study revealed that the hierarchy is *not* self-similar in these cool clouds down to sub-parsec scales, and that there is a preferred scale with clump masses of a few 100 M_{\odot} and sizes of about 1 pc. This seems different in warm molecular clouds, associated with sites of active star formation. Blitz (1987) demonstrates in a ¹³CO study that the cloud associated with the Rosette Nebula breaks up into ≈ 80 fragments, with a mass spectrum $dN/dM \propto M^{-1.5}$ over the range $18 < M/M_{\odot} < 2800$. In both these studies, the line width of individual clumps corresponds roughly to the one expected if the clumps are close to virial equilibrium. Recently, Loren (1989*a, b*) studied the ρ Ophiuchus complex in ¹³CO $J = 1 \rightarrow 0$ and identified 89 clumps with masses ranging between 0.6 and 844 M_{\odot} and a mass distribution $dN/dM \propto M^{-1.1}$.

In this paper we present a study of the M17 SW cloud core with the IRAM 30 m telescope, including maps in the molecular transitions of C¹⁸O $J = 2 \rightarrow 1$, C³⁴S $J = 3 \rightarrow 2$ and $2 \rightarrow 1$, and spectra of several isotopic species of these molecules in different transitions toward selected positions. Due to the small beam size available, these observations show *direct* evidence for the clumpy and macroturbulent structure of a giant molecular cloud core.

The M17 SW region (at a distance of 2.2 kpc: Chini, Elsässer, and Neckel 1980) is a typical giant molecular cloud core. The dense core lies adjacent to a prominent H II region (Felli, Churchwell, and Massi 1984). The complex is thus one of the prime examples of triggered star formation, where the H II region around the new high-mass stars that formed recently from the giant molecular complex compressed the adjacent molecular cloud material, thus initiating the formation of the next generation of stars. Several embedded objects, visible via their mid-IR emission (Kleinmann and Wright 1973; Harper *et al.* 1976) and H₂O maser activity (Lada *et al.* 1976; Jaffe, Güsten, and Downes 1981) indicate the presence of the next generation of very young stars embedded in the cloud.

The radio- and millimeter-wave molecular line studies of the M17 SW core have shown the presence of material with densities ranging between several 10^4 and 10^6 cm⁻³ (Snell *et al.*

1984, 1986; Evans *et al.* 1987; Mundy *et al.* 1986, 1987) and a temperature of the bulk of the material of around 50–70 K (Güsten and Fiebig 1988). These temperatures agree reasonably well with the range of temperatures derived from dust measurements (Gatley *et al.* 1979). The measurements indicate a temperature gradient away from the H II region, as would be expected if the cloud is heated externally by the H II region.

High-angular resolution radio continuum observation of the H II region (Felli, Churchwell, and Massi 1984) show small-scale structure interpreted to result from many high-density, neutral clumps with sizes of typically 10'' to a few times 10'' and masses of a few times 10 M_{\odot} embedded in the thin, ionized gas. Felli, Churchwell, and Mask point out that these clumps may represent the original structure of the molecular cloud. Due to their large density ($> 10^5$ cm⁻³), these clumps can survive over at least several 10^4 yr once the ionization front of the H II region has passed them.

II. OBSERVATIONS

Most of the observations were carried out on 1987 May 19–23 with the IRAM 30 m telescope on Pico Veleta, Spain. The observations were made in total power mode with typically 3×20 s on-source integration time per position. The off-source position ($\Delta\alpha = 500''$, $\Delta\delta = -300''$ offset from the reference position given below) was carefully selected to be emission free. Two sets of mapping observations were made, one using the 220 GHz and the 90 GHz Schottky receivers simultaneously to observe the C¹⁸O $J = 2 \rightarrow 1$ (219.560327 GHz) and the C³⁴S $J = 2 \rightarrow 1$ (96.412963 GHz) lines, the other using the 220 GHz Schottky receiver in parallel with the 140 GHz SIS receiver to observe the C¹⁸O $2 \rightarrow 1$ line simultaneously with the C³⁴S $J = 3 \rightarrow 2$ (144.617147 GHz) line. The alignment between the different receivers was determined to be better than 1''–2''. In addition, ¹³CO $J = 2 \rightarrow 1$ and $1 \rightarrow 0$, ¹²CO $J = 2 \rightarrow 1$, and C¹⁷O $2 \rightarrow 1$ as well as C³²S and C³⁴S $J = 5 \rightarrow 4$ and $2 \rightarrow 1$ spectra were taken toward several selected positions during later observing runs to better constrain the molecular excitation conditions. The observational parameters are listed in Table 1.

Complementary to the standard calibration procedure provided by the IRAM on-line software (hot-cold load measurements combined with a sky measurement to determine atmospheric transmission and the T_A^* scale; tabulated values for the beam efficiency to convert to a T_R or main-beam brightness temperature scale), we verified the calibration by observing Saturn in spectral line mode. With a disk diameter of 17''.4 at the time of the observation, and assuming a brightness temperature of 140 K at all three frequencies, these measurements confirm the calibration parameters provided by the IRAM on-line software within 10%. We quote all line temperatures in units of main-beam brightness temperatures (T_{mb} , not including the Planck correction, i.e., a Rayleigh-Jeans temperature scale), derived from T_A^* by dividing through the coupling effi-

TABLE 1
OBSERVING PARAMETERS

Line	Frequency (GHz)	Receiver	Θ_B (FWHM)	Back End	dv (km s ⁻¹)
C ¹⁸ O $J = 2 \rightarrow 1$	219.560	Schottky	13''	$\left\{ \begin{array}{l} 512 \times 1 \text{ MHz} \\ 128 \times 100 \text{ kHz} \end{array} \right.$	1.365 0.137
C ³⁴ S $J = 3 \rightarrow 2$	144.617	SIS	17	$128 \times 100 \text{ kHz}$	0.207
C ³⁴ S $J = 2 \rightarrow 1$	96.413	Schottky	27	$128 \times 100 \text{ kHz}$	0.311

ciency onto a disk source of approximately the size of the main diffraction beam. The thus defined T_{mb} scale is then equivalent to T_R as defined by Kutner and Ulich (1981), with a source coupling efficiency η_c appropriate for a main-beam size source. Due to the very close to Gaussian beam shape and the rather clean diffraction beam of the IRAM 30 m telescope at the observed frequencies, the temperature scale thus depends very little on the precise size of the calibration source (Saturn). Pointing scans of Saturn and several quasars were used to determine the beam shape and size given in Table 1 (using the method described in Harris 1988). If part of the diffraction beam of the telescope (sidelobes) hits a more extended source, the derived main beam brightness temperature will be an overestimate, including some of the extended source flux. Interpolation between measurements of the coupling efficiency to different size sources (planets and the Moon) shows that this may result in an overestimate by about (maximum) 20%, even in the pessimistic case of a uniform brightness source of $3'$ extent (Genzel *et al.* 1990). Further data reduction generally involved only the subtraction of linear baselines.

Figure 1 (Plate 11) gives an overview of the area observed. The position offsets in this paper are referred to the position of the SAO star 163157 at R.A.(50) = $18^h17^m34^s.5$, decl.(50) = $-16^\circ13'24''$. The $C^{18}O$ $J=2 \rightarrow 1$ map of the M17 SW molecular cloud covered a region of roughly $2' \times 3'$ extent (~ 280 points). The basic grid spacing was $15''$. The region along the ridge in M17 SW at the H II region/molecular cloud interface was additionally sampled at the points diagonally between. A region west of the 1.3 cm continuum arc in M17 SW (Felli, Churchwell, and Massi 1984) of $1' \times 1'$ extent was fully sampled on a 7.5 grid. The $C^{34}S$ $2 \rightarrow 1$ and $3 \rightarrow 2$ maps were obtained at subsets of these positions.

III. RESULTS

a) $C^{18}O$ $2 \rightarrow 1$ Mapping Observations

Figure 2 shows the velocity-integrated map of the $C^{18}O$ $J=2 \rightarrow 1$ emission from M17 SW. The morphology of the M17 SW cloud core is obviously much more complex when observed with high angular resolution in a rare isotope CO line than can be anticipated from lower angular resolution work (see, e.g., Thronson and Lada 1983 for a ^{13}CO $1 \rightarrow 0$ map with $50''$ angular resolution). The main features in the IRAM 30 m $C^{18}O$ $2 \rightarrow 1$ map are (1) a bright and narrow south-eastern ridge along the H II region/molecular cloud interface; (2) a prominent knot of emission about $30''$ west from the radio continuum arc (Felli, Churchwell, and Massi 1984, Fig. 1), which we will call the northern condensation; (3) a hole in the emission behind this knot, where a finger of radio continuum emission extends into the cloud; and (4) a significantly low emission area of about $1'$ diameter directly east of the embedded Kleinman-Wright IR source.

The integrated intensity distribution shows substantial spatial variations down to the scale of the beam size ($13''$ FWHM; corresponding to 0.14 pc at a distance of 2.2 kpc). These spatial variations are best depicted in individual velocity channel maps (Figs. 3a and 3b give representative examples). Comparison of maps for adjacent velocity intervals shows that the spatial distribution of the emission changes rapidly within 1.5 to 2 km s^{-1} . This can also be seen in position-velocity maps (Fig. 4).

We conclude that the molecular emission is clumpy on scales down to at least 0.14 pc and that the individual clumps have

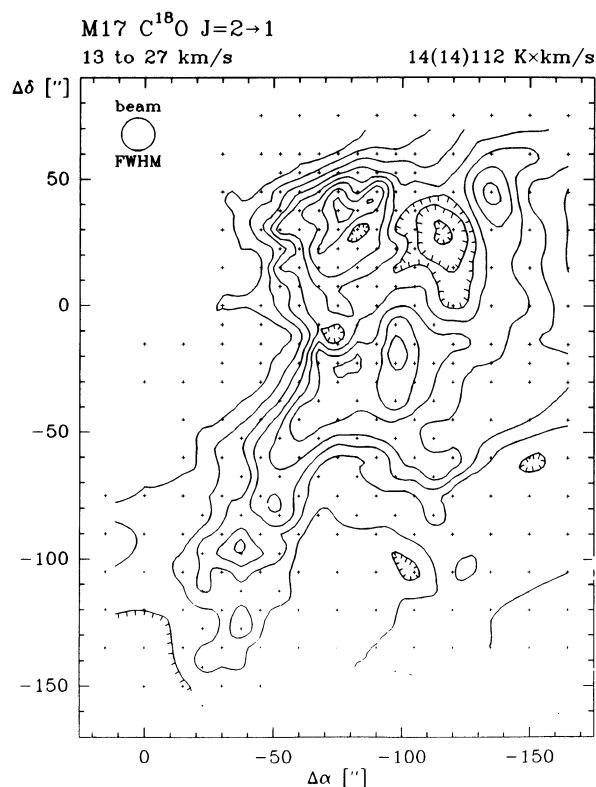


FIG. 2.—Velocity-integrated $C^{18}O$ $J=2 \rightarrow 1$ main-beam brightness temperature, integrated from $v_{LSR} = 13$ – 27 km s^{-1} . Contours are 14 – 112 K km s^{-1} in steps of 14 . The observing grid is superposed for comparison. The nominal offset position is the SAO star Number 163157 at R.A.(50) = $18^h17^m34^s.5$, decl.(50) = $-16^\circ13'24''$ (see Fig. 1).

line widths typically around 1 km s^{-1} (FWHM). The emission distribution shows several local maxima and at least two prominent depressions in the cloud core, where the intensity drops to about 20% of the peak. In particular, spots of recent star formation, identified either by their IR emission or by H_2O maser activity, are at the edges of the molecular cloud structures seen in $C^{18}O$ (see Fig. 1 and § IIc).

The very sharp rise in $C^{18}O$ $2 \rightarrow 1$ emission at the edge of the radio continuum emission region and the close correspondence between the CO and radio continuum contours on either side of the edge (Fig. 1) strengthen earlier indications (Icke, Gatley, and Israel 1980; Thronson and Lada 1983) that the interface is seen almost edge-on. Especially, the radio continuum emission, and thus the ionization front of the H II region, do not penetrate into the molecular cloud, despite of its clumpy structure. A small fraction of molecular material, traceable only in the main isotopic emission from CO, is also located along the line of sight toward the H II region. As shown by Rainey *et al.* (1987) in their ^{12}CO $J=3 \rightarrow 2$ study, this material probably takes part in an overall expansion motion, driven by the expanding ionization front of the H II region.

b) CO Line Comparison

The peak $C^{18}O$ $J=2 \rightarrow 1$ main-beam brightness temperature in the $13''$ beam is 23.6 K (at $\Delta\alpha, \Delta\delta = -76'', 38''$). Due to the small-scale structure of the emission, lower angular resolution observations are severely affected by beam dilution. For example, the $C^{18}O$ $J=2 \rightarrow 1$ peak main-beam brightness temperature at position $(-60, -30)$ is 13 K in our $13''$ beam.

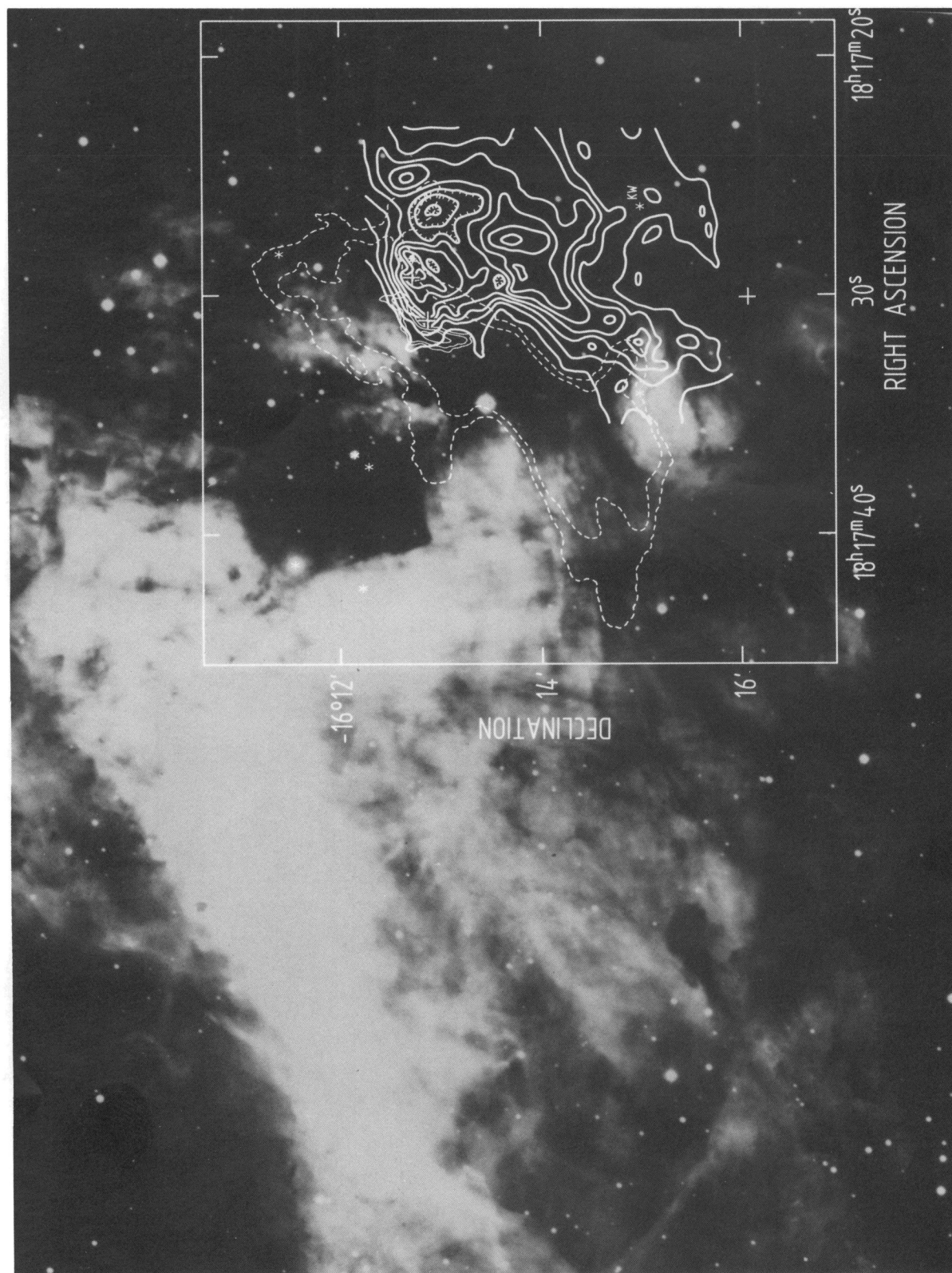


FIG. 1.—Velocity-integrated $C^{18}O$ $J = 2 \rightarrow 1$ emission (solid lines), superposed on an optical photograph of M17 SW (courtesy R. Chini). Contours are the same as in Fig. 2. Asterisks denote early-type stars that mainly contribute to the ionization of the complex (Chini, Eliasäcker, and Neckel 1980). Embedded H_2O masers (Jaffe, Güsten, and Downes 1981; thin crosses), the ultracompact H II region UC1 (Felli, Churchwell, and Massi 1984; thick cross), and the Kleinmann-Wright IR source (Kleinmann and Wright 1973) are indicated. The lowest contours of the extended 6 cm radio continuum (dash-dotted) and the 1.3 cm continuum arc (dotted; Felli, Churchwell, and Massi 1984) are given for comparison, both depicting the location of the M17 ionization front.

STUTZKI AND GÜSTEN (see 356, 515)

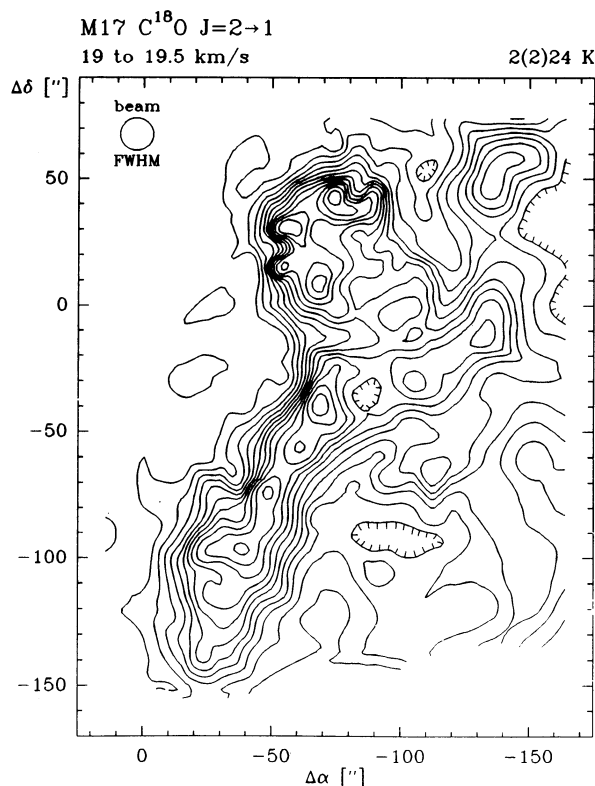


FIG. 3a

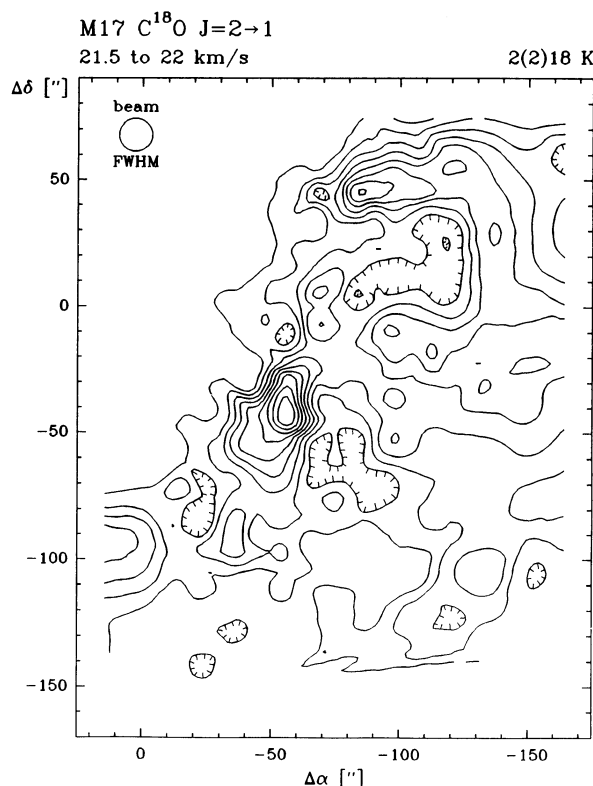


FIG. 3b

FIG. 3.—Representative channel maps of the M17 SW $\text{C}^{18}\text{O } J=2 \rightarrow 1$ emission, delineating the clumpy nature of the cloud in velocity space. The contours are in steps of 2 K, from 2 to 24 K, in units of main-beam brightness temperature, averaged over 0.5 km s^{-1} wide channels, centered at $v_{\text{LSR}} = 19.25$ and 21.75 km s^{-1} , respectively.

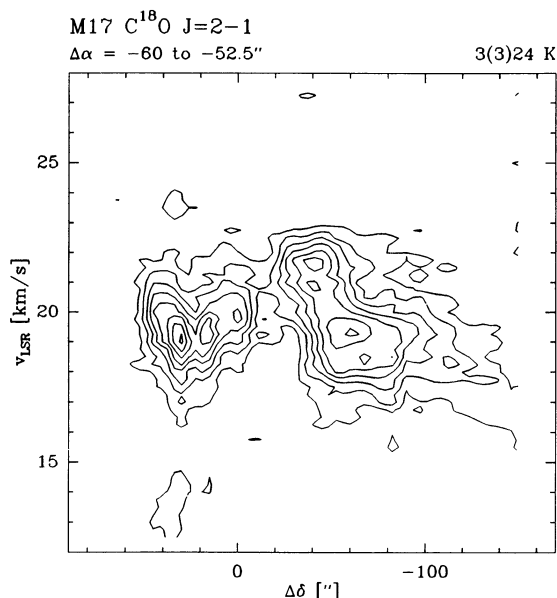


FIG. 4.—Typical declination-velocity diagram in the $\text{C}^{18}\text{O } J=2 \rightarrow 1$ transition, cutting through the northern condensation and the southern ionization front, averaged over a $7''.5$ wide strip at right ascension offset $\Delta\alpha = -56''$. Contours are in steps of 3 K main-beam brightness temperature from 3 to 24 K.

In the $30''$ FWHM beam of the NRAO 12 m telescope, it is only 8.4 K ($T_R^* = 7 \text{ K}$ from Stutzki *et al.* 1988, corrected up so that their T_R^* scale gives a $T_{\text{mb}} = 100 \text{ K}$ bright ^{12}CO line in Orion). For the $^{12}\text{CO } J=2 \rightarrow 1$ line at the same position, the difference is much bigger: when observed with the NRAO 12 m telescope (Stutzki *et al.* 1988), it shows a peak line temperature of $T_R^* = 45 \text{ K}$; in the IRAM 30 m telescopes $13''$ beam, it has a peak T_{mb} of 120 K (Fig. 5). This difference is certainly much larger than the calibration uncertainties, including overestimates of the intensity due to coupling of the extended ^{12}CO emission to the sidelobes of the beam. This is also supported by the fact that the ^{12}CO intensity observed with the IRAM 30 m telescope at other positions in the cloud core, e.g., $-120, -75$ (Fig. 6), is much lower. It is important to note that the difference cannot be due to a systematic, large difference in the calibration scheme of both telescopes: first, the intensity ratios are different between the ^{12}CO and C^{18}O observations; second, the intensity we obtain if we smooth our C^{18}O data to the NRAO 12 m telescope resolution agrees within 20% with the intensity measured there. The high temperature in a small beam is also confirmed by the $^{13}\text{CO } J=2 \rightarrow 1$ main-beam brightness temperature observed at the same position with the $13''$ IRAM 30 m beam, which is 60 K.

It is thus very important to only compare spectra observed with similar angular resolution. Also, a careful check and possible correction for even small pointing errors are essential for line comparison. At three selected positions, tracing the northern condensation, the cloud core, and the ridge bordering the ionization front, we have measured $J=2 \rightarrow 1$ spectra of the

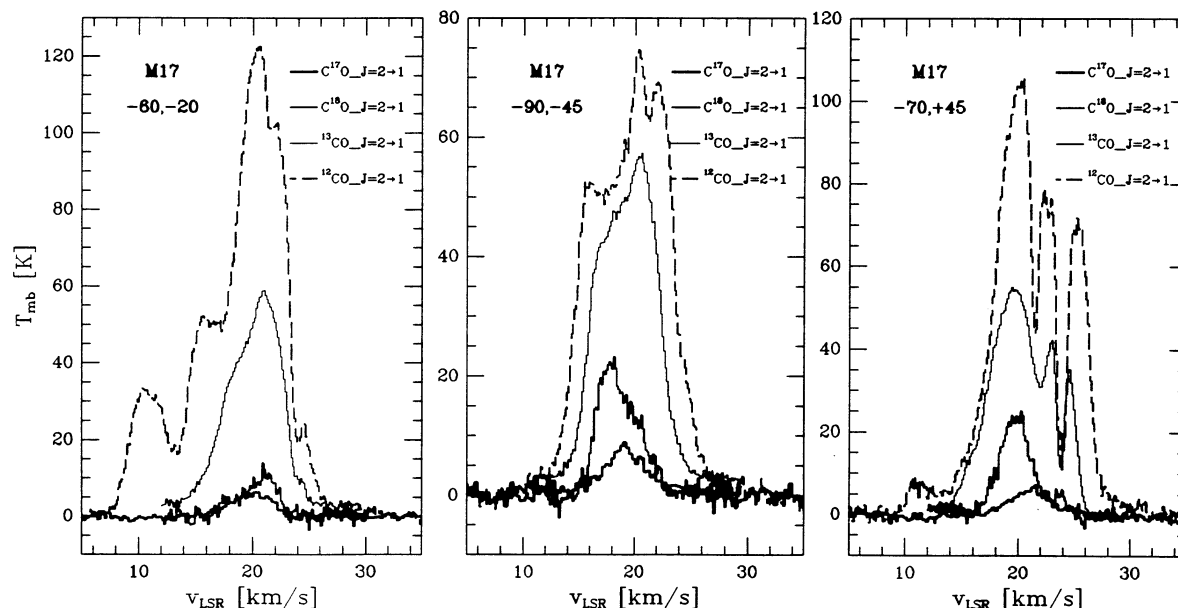


FIG. 5.—Line shape comparison of the isotopic CO $J = 2 \rightarrow 1$ transitions toward selected positions in the M17 SW cloud: (left) toward the H II region/molecular cloud interface (offset: $-69''$, $-20''$); (middle) the cloud core ($-90''$, $-45''$); and (right) the northern condensation toward the continuum arc ($-70''$, $+45''$). Note the high brightness of the ^{12}CO $J = 2 \rightarrow 1$ lines, and the partial correspondence between the C^{18}O emission features with the narrow, deep absorption notches seen in the ^{12}CO and ^{13}CO spectra. The slight difference between the C^{17}O and C^{18}O line profiles may in part be due to a slight pointing offset as discussed in the text.

four isotopes ^{12}CO , ^{13}CO , C^{18}O , and C^{17}O with the same angular resolution (Fig. 5). Comparison of the line profiles shows that both the main isotope line and the ^{13}CO line are heavily affected by self-absorption. In all three cases, the high-angular resolution ^{12}CO $2 \rightarrow 1$ line shows a very complicated profile with several absorption dips at the 20%–60% level with widths of 0.7 to a few km s^{-1} . The $30''$ FWHM observations with the NRAO 12 m telescope (Stutzki *et al.* 1988) do not show any similarly sharp and deep absorption features. It thus seems that the lower angular resolution profiles result from a spatial average over an intrinsically very bright ^{12}CO $2 \rightarrow 1$ emission with a rapidly varying pattern of deep and narrow self-absorption dips (except for, maybe, the $v_{\text{LSR}} = 24 \text{ km s}^{-1}$

feature visible at position offset $\Delta\alpha = -70''$, $\Delta\delta = 45''$, which is also seen in H_2CO [Bieging, Wilson, and Downes 1982] and NH_3 [Güsten and Fiebig 1988] and is probably related to a more extended, very cold foreground cloud). The resulting lower angular resolution profile is rather smooth, but it shows substantially lower intensity than the high-angular resolution observations.

The complex behavior of the CO intensity from different transitions and isotopes seems to be typical for several galactic and extragalactic sources (Genzel *et al.* 1990). M17 SW is just one example, and a possible interpretation, following the discussion by Genzel *et al.* (1990), is summarized in the following. The narrow, deep absorption features are suggestive of the presence of many small, cooler clumps in the cloud. Several absorption dips are related to emission features in the C^{18}O and C^{17}O $J = 2 \rightarrow 1$ lines. In other parts of the spectra, there seems to be no correspondence between the rare isotope emission features and the absorption dips. This is reasonable, since only some of the clumps will be located in front of the warm material causing the bright ^{12}CO and ^{13}CO lines. The bright ^{12}CO emission shining through in between the absorption dips implies the presence of gas with a kinetic temperature in excess of 120 K. The ^{13}CO lines seem to be not as heavily affected by self-absorption (except for position $-70, 45$), and their shape may give a good estimate of the intrinsic ^{12}CO profiles. The $^{13}\text{CO}/^{12}\text{CO}$ line ratio less than 1 in between the absorption notches indicates that this warm gas is still optically thin in ^{13}CO and has only moderate optical depth in ^{12}CO , although any such estimate is very uncertain because an estimate of the intrinsic intensity of the ^{12}CO line is very unprecise, given the complicated, self-absorbed profile.

The low- J ^{12}CO emission profiles, corrected for the self-absorption notches, thus indicate the presence of a small fraction of warm gas with substantially larger line width than the bulk of the material traced in the rare isotopes. Note, however, that this warm gas component is not visible in the much nar-

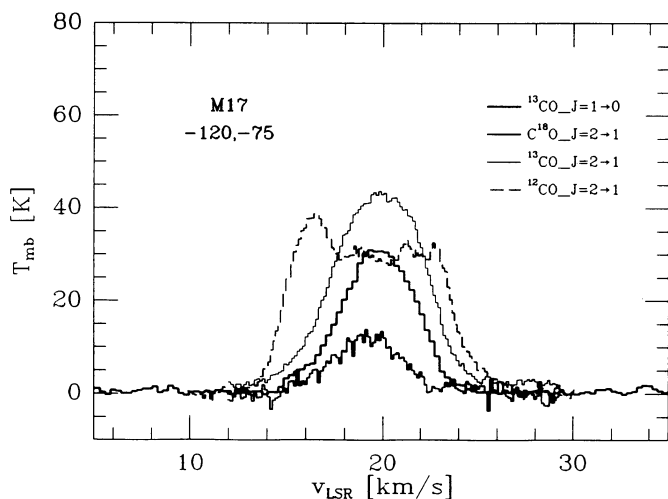


FIG. 6.—CO spectra toward a position near the embedded Kleinmann-Wright IR source (position offset: $-120''$, $-75''$). The isotopic ^{13}CO $J = 2 \rightarrow 1$ emission is stronger than the main isotope ^{12}CO $J = 2 \rightarrow 1$ line.

rower CO $J = 7 \rightarrow 6$ line profiles (Harris *et al.* 1987), which presumably arise from dense photodissociation regions on the surfaces of the clumps. The lower J emission probably originates in gas with low volume density (\approx a few 10^3 cm^{-3}), so that the $^{12}\text{CO } J = 7 \rightarrow 6$ line is not excited in this component. It may represent warm interclump gas, similar to that found by Blitz and Stark (1986) in the Rosette Nebula complex. The overall much larger column densities in the M17 SW core make this component close to optically thick, and thus bright in ^{12}CO emission from this source, whereas it is optically thin and therefore very weak in the case of the Rosette Nebula complex.

Another example for the effects of many small-scale, deep self-absorption features visible with high angular resolution are ^{12}CO , ^{13}CO , and $\text{C}^{18}\text{O } J = 2 \rightarrow 1$ spectra toward position $(-120, 75)$ in the vicinity of the embedded Kleinman-Wright source. Whereas the lower angular resolution spectra in this area show a smooth, somewhat flatter than Gaussian, broad ^{12}CO line (see, e.g., Schulz, Gillespie, and Krügel 1985, and references therein), the high-angular resolution spectrum shows a wiggly top with the intensity peak blueshifted with respect to the line center. The ^{13}CO profile, however, is smooth, almost Gaussian-shaped, with a peak intensity about 25% brighter than the ^{12}CO line (Fig. 6).

There is evidence that even the $\text{C}^{18}\text{O } 2 \rightarrow 1$ line is moderately optically thick in some places. This is already implied by the rather high $\text{C}^{18}\text{O } J = 2 \rightarrow 1$ peak brightness temperature (24 K) compared to the average kinetic temperature of the bulk material ($\approx 50 \text{ K}$). The optical depth of the C^{18}O line can be determined by comparison with the C^{17}O line intensity. The $\text{C}^{17}\text{O } J = 2 \rightarrow 1$ line shows nuclear quadrupole hyperfine splitting. Most of the intensity is grouped in three roughly equidistant components spreading over 1.5 km s^{-1} (Lovas and Krupenie 1974) and is thus not resolved in the spectra shown in Figure 5. A direct comparison of the C^{18}O and C^{17}O line intensities has to take into account that at least some of the intensity variations across the profiles are certainly due to small pointing differences between the independent observations, which together with the extremely small scale source structure can cause very different looking profiles. At none of the positions observed in $\text{C}^{17}\text{O } 2 \rightarrow 1$ do the C^{18}O and C^{17}O profiles fully match. At the three positions where we obtained $\text{C}^{17}\text{O } J = 2 \rightarrow 1$ spectra, the $\text{C}^{18}\text{O}/\text{C}^{17}\text{O}$ line intensity ratio varies between about 1.0 and 6.0 across the spectra. If this variation is due to optical depth effects, and assuming an interstellar isotopic abundance ratio of $[\text{C}^{18}\text{O}]/[\text{C}^{17}\text{O}] \approx 4$ (Penzias 1981), this implies a range of optical depths in the $\text{C}^{18}\text{O } J = 2 \rightarrow 1$ line from optically thin to about 4 across the line.

c) CS Observations

Due to lower angular resolution, the C^{34}S maps do not show that many details of the source structure. However, velocity-integrated emission maps, but also individual channel maps of the $\text{C}^{34}\text{S } J = 2 \rightarrow 1$ and $J = 3 \rightarrow 2$ emission, look very similar to the $\text{C}^{18}\text{O } J = 2 \rightarrow 1$ maps, if the latter is smoothed to the same angular resolution (Fig. 7). Line shapes are quite comparable (Fig. 8). The $\text{C}^{18}\text{O } J = 2 \rightarrow 1$ and C^{34}S emission must therefore have very similar spatial distribution. In particular, there is no indication that the C^{18}O emission (tracing column density) is more extended than the C^{34}S emission (tracing high density). This suggests that most of the column density in the cloud core is contributed by high-density,

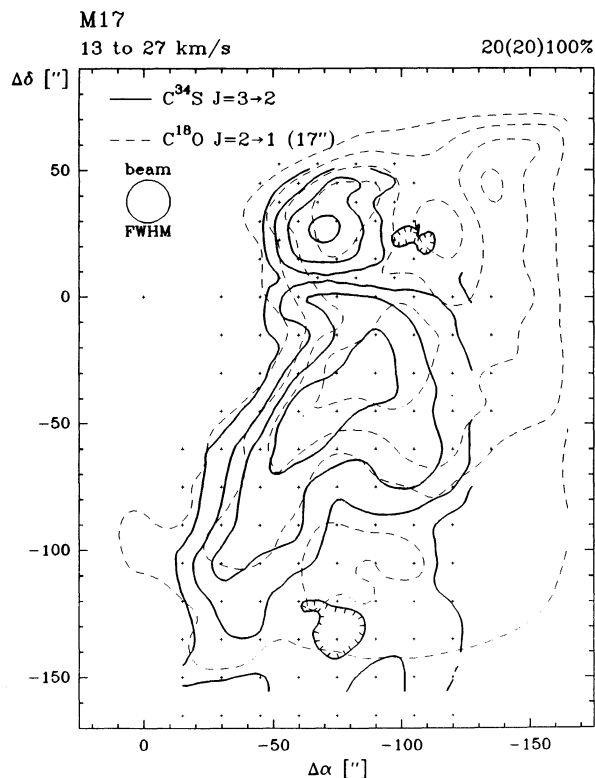


FIG. 7.—Distribution of the $\text{C}^{34}\text{S } J = 3 \rightarrow 2$ and $\text{C}^{18}\text{O } J = 2 \rightarrow 1$ emission, integrated in the velocity range $14\text{--}26 \text{ km s}^{-1}$. Contours are in 20% steps of the peak intensity for both maps (peak: 27 K km s^{-1} for $\text{C}^{34}\text{S } J = 3 \rightarrow 2$ and 125 K km s^{-1} for $\text{C}^{18}\text{O } J = 2 \rightarrow 1$, respectively). The C^{34}S observing grid is marked by light crosses. The C^{18}O emission has been smoothed to the $17''$ beam of the CS measurements.

clumpy gas. There is no indication of a lower density, more extended halo around these clumps.

The CS $J = 7 \rightarrow 6$ map published by Snell *et al.* (1986) is remarkably similar to the $\text{C}^{34}\text{S } 3 \rightarrow 2$ isotopic, optically thin emission map presented here, considering the poorly defined beam pattern of the MMT ($27''$ main beam, with strong sidelobes in a hexagonal pattern). In contrast to CO, it thus seems that the CS lines from different J levels and different isotopes all trace the same dense gas (that also seems responsible for the bulk of the $\text{C}^{18}\text{O } J = 2 \rightarrow 1$ emission). This is emphasized by the similarity of individual spectra of different CS, C^{34}S , and C^{18}O transitions (Fig. 8).

IV. DISCUSSION

a) Physical Parameters of the Emitting Gas

i) C^{18}O : Total Column Density

In the optically thin, thermalized limit, the C^{18}O line intensity is proportional to column density and inversely proportional to temperature. The actual variation with temperature is much weaker because the excitation drops rapidly below the thermalized limit for transitions with critical densities greater than the cloud density, which effectively limits the number of available molecular states at higher temperature (see Stutzki, Genzel, and Harris 1990 for a detailed discussion). In addition to the weaker temperature dependence, the subthermal excitation of higher levels also results in an overestimate of total column densities in the optically thin, thermalized limit. In addition, the high observed peak main-beam bright-

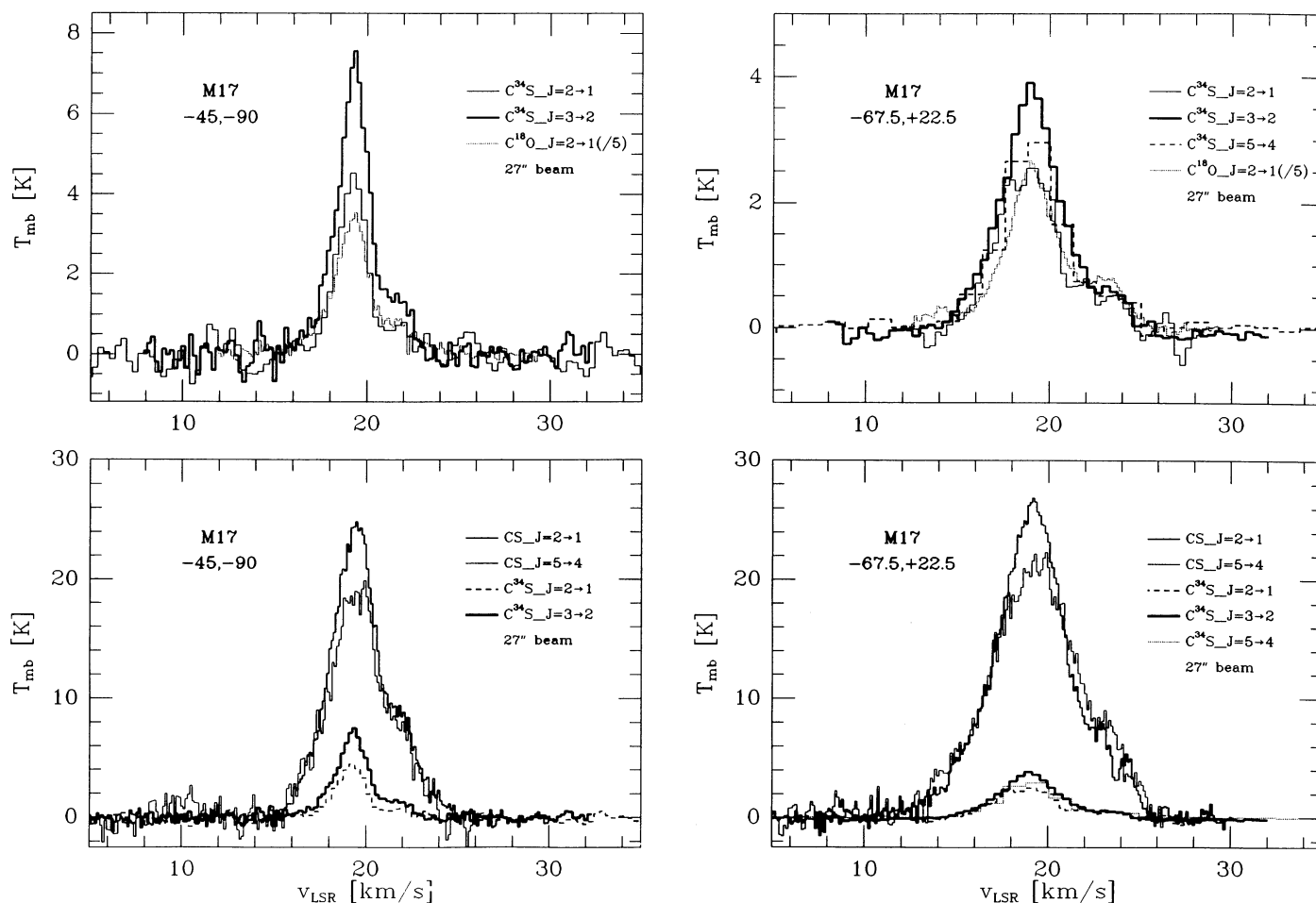


FIG. 8a

FIG. 8b

FIG. 8.—Comparison of main-beam brightness temperature and line shape of CS, $C^{34}S$, and $C^{18}O$ $J = 2 \rightarrow 1$ spectra, taken (a) close to the peak of the northern condensation ($-67.5, +22.5$) and (b) toward the south-eastern ridge bordering the ionization front ($-45, -90$). All spectra have been smoothed to the $27''$ resolution of the CS $J = 2 \rightarrow 1$ measurements. The $C^{18}O$ intensity scale is reduced by a factor of 5, for comparison.

ness temperatures of the $C^{18}O$ $J = 2 \rightarrow 1$ line imply that the emission has to be moderately optically thick in some places, even for this rare isotope. Optical depth effects, which lead to an underestimate of the column density derived in the optically thin, thermalized limit, thus have to be taken into account.

Radiative transfer calculation in a single component escape probability model (Stutzki and Winnewisser 1985) show that the observed peak line temperature of 24 K corresponds to a $C^{18}O$ column density per velocity interval between 2.5 and $3.5 \times 10^{16} \text{ cm}^{-2}/(\text{km s}^{-1})$, pretty much independent of the kinetic temperature (over the range 40–120 K). This value is very close to the one derived in the optically thin, thermalized limit for a kinetic temperature of 50 K. These numerical results show that the effects of subthermal excitation in the higher levels and slight optical depth in the observed $2 \rightarrow 1$ transition almost cancel.

Because of the weak temperature dependence of the derived column densities, the structure visible in the $C^{18}O$ $J = 2 \rightarrow 1$ emission is due mainly to column density structure in the source, rather than temperature variations. The similarity of the $C^{34}S$ emission distribution with the $C^{18}O$ distribution suggests that the strong $C^{18}O$ emission actually arises from high-density regions.

Although detailed knowledge of the kinetic temperature is thus not required to derive accurate values for the column density from the observed $C^{18}O$ $J = 2 \rightarrow 1$ brightness, we want to briefly discuss the temperature in the cloud core. The kinetic temperature structure across the M17 SW molecular cloud is complex, and components with quite different temperatures seem to exist along the same line of sight. A characteristic temperature for the bulk of the material is $50 \pm 15 \text{ K}$, as derived from both dust continuum measurements (Gatley *et al.* 1979) and excitation studies of the ammonia molecule (Güsten and Fiebig 1988). The temperature regularly decreases with increasing distance from the ionization front, with T_{kin} as low as 30 K in remote sections of the cloud (e.g., close to the KW IR source) but $T_{\text{kin}} \geq 60 \text{ K}$ in the northern condensation just bordering the ionization front. Below, from fitting the CS excitation, kinetic temperatures of 50–70 K are required.

We want to emphasize that the agreement between this bulk temperature and the average ^{12}CO brightness temperature (observed in lower resolution studies) seems to be accidental. The high-angular resolution spectra (see above) show that the mean ^{12}CO brightness temperature results from a spatial average over complicated, self-absorbed profiles with peak intensities of up to 120 K and absorption dips down to as low

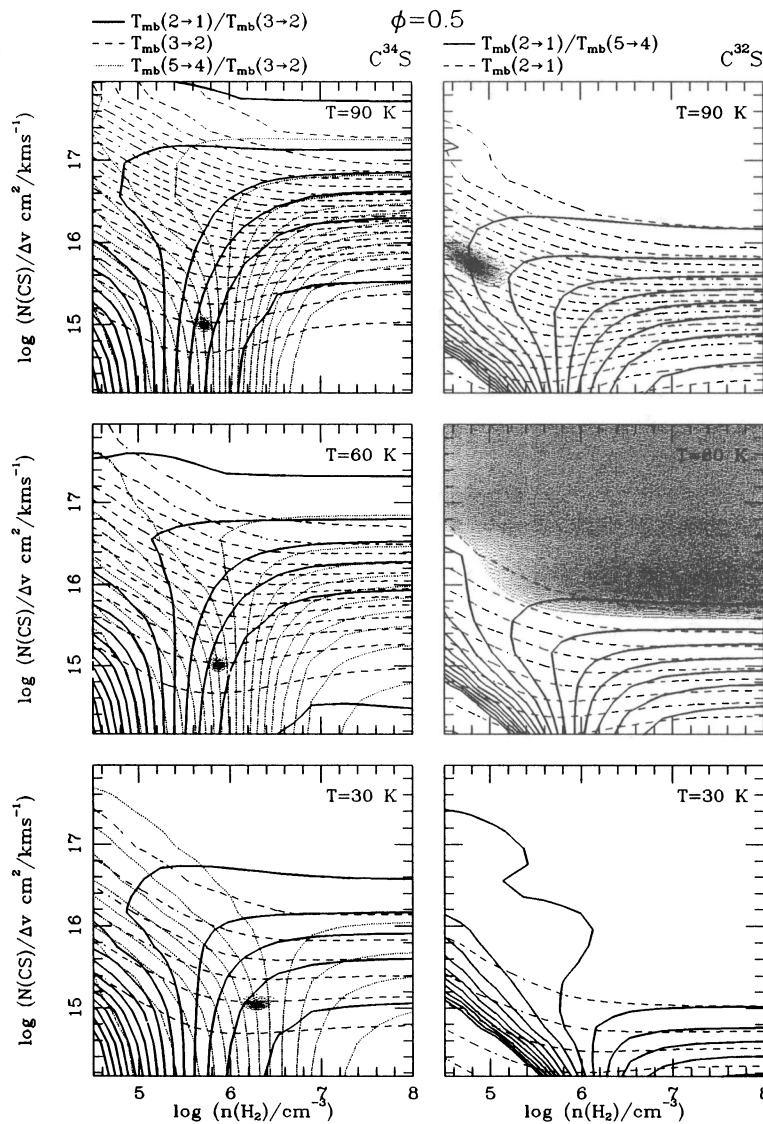


FIG. 9a

as 30 K. With the large column densities involved, already tiny fractions of the total column density become optically thick in ^{12}CO and thus show a ^{12}CO line brightness temperature equal to the local temperature at this location.

With the value for column density per velocity interval discussed above, the observed peak integrated $\text{C}^{18}\text{O } J = 2 \rightarrow 1$ emission in M17 SW of 125 K km s^{-1} at position $(-97.5, -22.5)$ corresponds to a beam averaged C^{18}O column density of $1.3 \times 10^{17} \text{ cm}^{-2}$. The optical depth of the 4.8 km s^{-1} wide line corresponding to this beam-averaged column density is ≈ 0.7 . Since the source shows structure on the scale of the beam size, the source-intrinsic optical depth will be slightly higher than the one derived from the beam-averaged column density. The $\text{C}^{18}\text{O } J = 2 \rightarrow 1$ optical depth estimated here thus agrees well with the one indicated above by the $\text{C}^{18}\text{O}/\text{C}^{17}\text{O}$ line comparison.

With an isotopic abundance of C^{18}O of $1/500$ and a CO abundance of 8×10^{-5} , the C^{18}O peak column density derived above corresponds to a beam-averaged molecular hydrogen column density of $8.1 \times 10^{23} \text{ cm}^{-2}$. The intensity

FIG. 9.—Radiative transfer analysis of the CS and C^{34}S lines: constant line brightness ratio contours are shown vs. H_2 volume density and CS (main isotope) column density at three different kinetic temperatures (30, 60, and 90 K; bottom to top) for C^{34}S (left-hand side) and CS (right-hand side) lines. Panels (a) and (b) are the same as far as the contour levels are concerned. The plots assume a $\text{CS}/\text{C}^{34}\text{S}$ line ratio of 22.6. The dashed $\text{C}^{34}\text{S } T_{\text{mb}}(3 \rightarrow 2)$ and CS $T_{\text{mb}}(2 \rightarrow 1)$ contours in each panel start at the bottom with a level of $T_{\text{mb}} = 4 \text{ K}$ and increase in steps of 0.1 K to the top. The line ratio contours increase in steps of 0.1 from right to left ($2 \rightarrow 1/5 \rightarrow 4$ and $2 \rightarrow 1/3 \rightarrow 2$), respectively left to right ($5 \rightarrow 4/3 \rightarrow 2$), with the contour at a level of 1.0 being the first contour bending all the way to the right. The gray shading, i.e., the density of dots, in each plot is proportional to $\exp(-\chi^2)$, i.e., the probability that the observed intensities of the three C^{34}S lines (left) and the two C^{32}S lines (right) at position $(-67.5, +22.5)$ (Fig. 8a) are fitted by the conditions in that part of the density-column density plane, assuming a beam filling factor of (a) 1.0 and (b) 0.5. Note that the most likely (gray shaded) areas for the isotopic lines (left side) and main isotope lines (right side) do not overlap well, except for the case of a beam filling factor close to unity.

integrated over the area of our map gives a total mass of $1.45 \times 10^4 M_{\odot}$. This is in remarkable agreement with the virial mass estimate given by Snell *et al.* (1984), $1 \times 10^4 M_{\odot}$. Assuming that the line-of-sight extent of the cloud is of similar size as the extension along the H II region/molecular cloud interface (3.3 or 2.1 pc), this mass corresponds to an average H_2 volume density over the area observed of $3.7 \times 10^4 \text{ cm}^{-3}$.

ii) CS: Column Density of High-Density Gas

The observed peak $\text{C}^{34}\text{S } J = 3 \rightarrow 2$ integrated intensity of 27 K km s^{-1} at position $(-60, -45)$ requires a beam-averaged column density in C^{34}S of $1.6 \times 10^{14} \text{ cm}^{-2}$ in the optically thin, thermalized limit at a kinetic temperature of 50 K. The effects of subthermal excitation in higher levels, discussed above for CO, are even more important for CS with its much higher critical density. The radiative transfer analysis (see below and Fig. 9) shows that this value, derived in the optically thin and thermalized limit, is an overestimate by about 50% (even at the very high densities of 10^6 cm^{-3}). We therefore assume a beam-averaged peak C^{34}S column density of

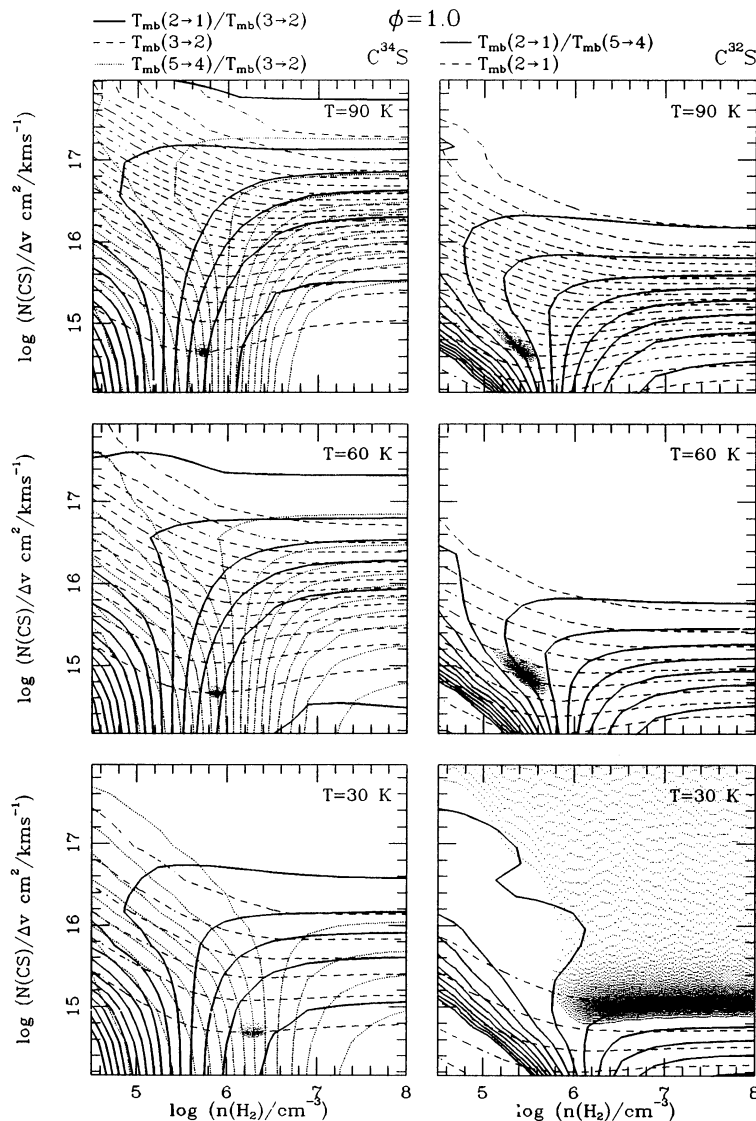


FIG. 9b

$8 \times 10^{13} \text{ cm}^{-2}$, which, due to the subthermal excitation of higher rotational levels, is again largely independent of the assumed kinetic temperature in the cloud (see Fig. 9). Values close to the peak integrated emission in the northern core are also found across the core region near $(-90'', -40'')$, which extends over 1.5 by 1.5. The derived values for the column density are thus in good agreement with the peak values derived by Mundy *et al.* (1986) from their 1' angular resolution observations.

The terrestrial isotopic abundance ratio $^{32}\text{S}/^{34}\text{S}$ is 22.6. The $[\text{CS}]/[\text{H}_2]$ abundance is not very precisely known and seems to depend on the astrophysical environment. In the Orion core, it varies between 2.5×10^{-9} for the quiescent ridge gas and 2×10^{-8} for the hot core component (Blake *et al.* 1987). Assuming the lower abundance to be characteristic for the M17 SW gas, the velocity-integrated peak intensity of $\text{C}^{34}\text{S } J = 3 \rightarrow 2$ corresponds to a peak molecular hydrogen beam averaged column density of $6.3 \times 10^{23} \text{ cm}^{-2}$. Thus, the amount of material probed by the high-density tracing C^{34}S lines is quite comparable to the amount of material probed by

the $\text{C}^{18}\text{O } J = 2 \rightarrow 1$ line, tracing column density. This is consistent with most of the $\text{C}^{18}\text{O } 2 \rightarrow 1$ emission originating in high-density material.

iii) CS: Excitation Conditions, Density, and Temperature

The critical density necessary for excitation of the different CS millimeter-wave transitions ranges from $\sim 10^5 \text{ cm}^{-3}$ to a few times 10^6 cm^{-3} , and the excitation of the optically thin C^{34}S lines is not influenced by trapping. We used a one-component escape probability radiative transfer program (Stutzki and Winnewisser 1985) to determine temperature, density, and column density from the different CS lines observed. The radiative transfer code models spherically symmetric, homogeneous clumps with a Gaussian line profile. Due to the large column densities in M17 SW, the main isotopic lines are likely to be optically thick. We will therefore first concentrate on the optically thin C^{34}S lines to derive limits on the gas density and temperature from these lines. In a second step, we will check whether the main isotopic lines are consistent with these estimates and what additional constraints they

give. In a third step, we then discuss what appears to be a strong indication for the inadequacy of a single-component radiative transfer model to explain all observed CS and isotopic CS lines.

After smoothing the $J = 3 \rightarrow 2$ data to the lower angular resolution of the $J = 2 \rightarrow 1$ data, the observed $\text{C}^{34}\text{S } J = 2 \rightarrow 1/3 \rightarrow 2$ line ratio varies typically between a value of 0.6–0.9 over the region mapped and also across the line profile at individual positions. The lower values are representative for the regions where the C^{34}S spectra show narrower lines [e.g., position (–45, –90), Fig. 8a], sometimes on top of a slightly wider line. The wider line component shows a ratio closer to unity. Spatially, the (comparatively) stronger $3 \rightarrow 2$ lines are confined to the cloud layers bordering the ionization front, namely the south-eastern ridge and the eastern boundary of the northern condensation.

As shown in Figure 9 (ignore the gray shading for the moment), $\text{C}^{34}\text{S } 2 \rightarrow 1/3 \rightarrow 2$ ratios (solid contours, Fig. 9, left side) around 0.6–0.7, typical for the observed range of intensity ratios, constrain the density in the emitting gas to be greater than 10^6 cm^{-3} for temperatures up to 70 K. At even higher temperatures (up to 100 K), slightly lower densities ($> 5 \times 10^5 \text{ cm}^{-3}$) are allowed. Densities close to the lower limit quoted are present if the observed emission fills the beam, i.e., the intrinsic $\text{C}^{34}\text{S } 3 \rightarrow 2$ brightness (dashed contours, Fig. 9a, left side) is close to the observed one of 4–6 K. If the emission is clumpy, i.e., the intrinsic brightness temperature of the $\text{C}^{34}\text{S } 3 \rightarrow 2$ line is higher than the observed beam diluted intensity, the volume density can be correspondingly higher, following the turnover from the vertical branch to the horizontal branch of the constant line ratio contours (Fig. 9b, left). Much higher densities (10^7 – 10^8 cm^{-3}) are required at lower temperatures (30–50 K) for beam filling factors below ≈ 0.6 in order to match the observed $2 \rightarrow 1/3 \rightarrow 2$ line ratio.

Complementary information from higher J transitions is needed to better constrain the solution. We have obtained a $\text{C}^{34}\text{S } J = 5 \rightarrow 4$ spectrum toward the northern condensation (–67.5, +22.5). The $\text{C}^{34}\text{S } 5 \rightarrow 4/3 \rightarrow 2$ ratio (dotted contours, Fig. 9, left side) of 0.80 shows that, at least at this position, the density is below $3 \times 10^6 \text{ cm}^{-3}$ even for the lower kinetic temperature range (see Figs. 9a, 9b, left side; the gray shading marks the region allowed by the constraints from all three C^{34}S lines). If the $\text{C}^{34}\text{S } J = 5 \rightarrow 4$ line is brighter at other positions, higher densities together with lower beam filling factors are also possible. A lower $\text{C}^{34}\text{S } J = 5 \rightarrow 4$ brightness toward other positions would be in conflict with the large $\text{C}^{34}\text{S } 3 \rightarrow 2/2 \rightarrow 1$ ratio observed everywhere in the source.

At the two positions where we have observations of the main isotope CS $J = 5 \rightarrow 4$ and $2 \rightarrow 1$ lines (Fig. 8), these lines have an intensity ratio of about unity. Only in the line center is the $5 \rightarrow 4$ line lower by about 15%. The right-hand sides of Figures 9a and 9b show the constraints imposed by the main isotopic lines via radiative transfer calculations. The observed CS $2 \rightarrow 1/5 \rightarrow 4$ line ratio (solid contours, Fig. 9, right side) of 0.9–1.0 gives density constraints not much different from the isotopic $\text{C}^{34}\text{S } 2 \rightarrow 1/3 \rightarrow 2$ line ratio discussed above. From the line ratio alone, the density can be anywhere higher than $\approx 10^6 \text{ cm}^{-3}$. Trapping in the main isotopic line helps to reduce the otherwise higher critical density of the $5 \rightarrow 4$ transition to a regime similar to that for the optically thin isotopic lower J transitions.

The 25 K peak main-beam brightness temperature of the main isotope $2 \rightarrow 1$ line (dashed contours, Fig. 9, right side) favors the lower density regime in case the emission fills the

beam (gray shading, Fig. 9a, right side), and the regions allowed by both the CS and C^{34}S observations actually overlap. Lower beam filling, pushing the intrinsic main line intensity up, results in an allowed parameter regime that does not agree at all with the constraints given by the isotopic lines (gray shading, Fig. 9b, right side).

The combination of all observed CS and C^{34}S lines can thus only be fitted with a beam filling factor close to unity and the density close to 10^6 cm^{-3} at a temperature of 50–90 K. Note that the $J = 5 \rightarrow 4$ $\text{C}^{32}\text{S}/\text{C}^{34}\text{S}$ brightness temperature ratio of ≈ 7 , together with the assumed isotopic abundance ratio of 22.6, implies an optical depth ≈ 3.5 for the main isotopic line. The $\text{C}^{32}\text{S } J = 5 \rightarrow 4$ brightness temperature of 21 K is nevertheless substantially lower than the kinetic temperatures mentioned above because of the subthermal excitation of this transition even at a density of 10^6 cm^{-3} .

NH_3 observations by Güsten and Fiebig (1988) imply a beam filling factor of ≈ 0.15 in a $40''$ (FWHM) beam for the ammonia emission from the northern condensation. This is in conflict with the filling factor close to unity in a $27''$ (FWHM) beam derived above from the main isotopic CS lines for dense gas, that should also emit strongly in ammonia. The difference may partly be due to chemical effects. However, the comparison between the mean density in the cloud, derived above from the C^{18}O data, and the density derived here, necessary for the excitation of the CS lines, indicates that the emitting gas must be clumpy. The isotopic C^{34}S observations alone would allow for a lower beam filling factor (≈ 0.5) of the CS emitting gas. The discrepancy may thus be taken as a strong indication that at least the main isotopic CS lines have to be explained by emission from gas with a range of densities and temperatures, where cooler and/or less dense outer layers partially absorb the higher J line radiation from the dense and warm clump cores. This is also indicated by the too-low intensity of the CS $5 \rightarrow 4$ line in the line center which may be attributed to self-absorption in the same less dense or cooler envelope of the clumps along the line of sight.

Further evidence for the need of a more complicated radiative transfer model to describe especially the main isotopic emission comes from comparing our high-angular resolution results with those derived by Snell *et al.* (1984) from their $1'$ resolution data. The densities derived in both cases are quite similar. However, a closer inspection shows that the data on which both estimates are based are quite different. For one, the intensities observed by Snell *et al.* (1984) are about a factor of 2 lower, presumably because of beam dilution in the much larger ($1'$ FWHM) beam. These lower intensities result in a lower estimated column density (Snell *et al.* 1984 determined a source-intrinsic peak CS column density of about $5 \times 10^{14} \text{ cm}^{-2}$, whereas the much brighter peak intensity we observed for the $\text{C}^{34} 3 \rightarrow 2$ line requires already a minimum CS column density of $1.5 \times 10^{15} \text{ cm}^{-2}$). Also, the intensities observed by Snell *et al.* (1984) in the higher J lines usually drop substantially below the values in the lower J lines. For example, the CS $5 \rightarrow 4/2 \rightarrow 1$ ratio observed at their peak intensity position (0, 1) is about 0.65, compared to 0.85 in our high-angular resolution data (not correcting for the likely self-absorbed dip in the line center). Nevertheless, the density required in both cases to explain the observed ratios and intensities is very similar because the requirement for higher densities to explain the high $5 \rightarrow 4/2 \rightarrow 1$ ratio in our data is compensated by the higher optical depth, that helps to excite the higher J lines via trapping.

This discrepancy in the line ratios observed with low and

high angular resolution supports the conclusion that a single-component model is not adequate to interpret the data, a conclusion also arrived at by Mundy *et al.* (1986) in interpreting their $C^{34}S$ $2 \rightarrow 1$, $3 \rightarrow 2$, and $5 \rightarrow 4$ low-angular resolution data. Density structure in the clumpy cloud, with high-density cores ($\geq 10^6 \text{ cm}^{-3}$) and less dense envelopes ($\approx 10^5 \text{ cm}^{-3}$) will result in the observed increase of high- J lines, that trace higher densities, in higher angular resolution observations, especially of isotopic lines.

To summarize, the $C^{34}S$ $J = 3 \rightarrow 2$ and $2 \rightarrow 1$ isotopic line ratio constrains the density to around 10^6 cm^{-3} or higher over the whole area of the cloud core. Detailed analysis, including main isotopic spectra at selected positions, and comparing lower and higher angular resolution data, shows that a more complicated radiative transfer analysis, including density and temperature gradients along the line of sight, is needed to explain the optically thick main isotope lines.

b) Physical Characteristics of the Clumpy Distribution of Molecular Material

In the previous sections, we have demonstrated that the molecular emission from the M17 SW cloud core originates in high-density material with small-scale spatial and velocity structure. In this section, we will attempt to further characterize the clumpy distribution of the molecular material, namely: What are the typical sizes and line widths of individual clumps? What are their column densities and average densities? And, most important, what are their masses and what is the mass distribution of the clumps?

To achieve this goal, we developed the clump fitting procedure described in detail in the Appendix. We assume that the source consists of many clumps, each clump having a Gaussian-shaped density distribution both in the two spatial and the velocity coordinates. The clumps are allowed to have an internal velocity gradient and arbitrary spatial orientation. The assumption of clumps with Gaussian shape is, of course, ad hoc and mainly motivated by the simple mathematical formulation (e.g., all projections have Gaussian shape, so that the column density, i.e., brightness distribution, is Gaussian as well). Also, fitting Gaussian distributions to clumps of other shape will still give useful values on many clump parameters such as typical sizes, velocity widths, etc. We investigated some of these effects by using the clump decomposition procedure on a set of synthesized clumps with circular shape and constant brightness (see the Appendix). In any case, any assumed shape of the clumps has to result in a rather sharp clump boundary, because otherwise the emission of a large number of clumps in a finite volume would lose its clumpy appearance.

The observed intensity distribution (main-beam brightness temperature as a function of two spatial and one velocity coordinate) was decomposed into individual Gaussian components in the following way: a Gaussian-shaped clump was fitted to the maximum of the map, with constraints to keep the position and amplitude of the fitted clump close to those of the map maximum, and with a (Gaussian) weighting of the map points decreasing with distance from the clump center position. This weighting emphasizes the small-scale structure rather than the large-scale distribution, and it prevents the fitting procedure from fitting a grand total average to the whole cloud in the first step. The fitted clump was then subtracted from the map and the process iterated until the integrated intensity of all fitted clumps was equal to the original integrated intensity

of the map. At this step, the peak fluctuations in the residual map correspond to about 5 times the rms of the data.

Following this procedure, the $C^{18}O$ $J = 2 \rightarrow 1$ emission in the observed field was decomposed into the contributions from 179 individual clumps. Although this number may seem large, inspection of the representative channel maps shown in Figure 3 and the position velocity cut shown in Figure 4, and an attempt to count the immediately visible clumps in these maps, shows that the number is not at all unreasonable. The large number of clumps was in fact motivation for developing the numerical clump deconvolution procedure, after initial attempts to identify the clumps by hand from a stack of channel maps pretty soon proved to be impractical.

Table 2 lists the fitted parameters for the clumps. It is clear that the decomposition into individual clumps is to some extent not unique, in particular for the weakest clumps, so that values for individual, weak clumps out of Table 2 should be used with some caution. The tests we did with synthesized clump distributions as described in the Appendix show that this kind of confusion mostly occurs when two or more clumps really sit that close to each other (both in spatial coordinates and velocity) that they almost merge.

i) Distribution of Clump Size, Velocity Width, and Intensity

In Figure 10, the distribution of fitted intrinsic clump size $\Delta\xi$ (FWHM size, geometrical mean of major and minor axis, and beam deconvolved; see Appendix), line width Δv , and intrinsic peak intensity T_0 (corrected for beam dilution) are displayed. Note that the observing procedure (spatial grid and limited spatial resolution and sensitivity) restricts the reliable part of these distributions to about $\Delta\xi > 10''$ and $T_0 > 5 \text{ K}$. Much smaller clumps would be impossible to deconvolve from the $13''$ beam, and intrinsic brightness temperatures lower than about 5 times the noise in the original map are ignored due to the finite number of iterations. The derived velocity dispersion distribution with the sharp falloff below 1 km s^{-1} is not significantly affected by the 0.5 km s^{-1} wide channels used in the fitting procedure. Simulations with synthesized data (see Appendix) show an increase of the width distribution down to the spectral resolution of the resampled data (0.5 km s^{-1}). The peak at 1 km s^{-1} thus seems to be an intrinsic property of the clump distribution. It is higher than the thermal line width of $C^{18}O$, $\Delta v_{\text{therm}} = 0.27 \text{ km s}^{-1} \times (T/50 \text{ K})^{1/2}$, but close to the line width expected for sonic turbulence, $\Delta v_{\text{sonic}} = 1.3 \text{ km s}^{-1} \times (T/50 \text{ K})^{1/2}$. The clumps thus are suprathermal, but for most of the clumps the additional turbulence seems to be subsonic.

ii) Area Filling Factor

Summing up the area corresponding to the intrinsic FWHM extent of the fitted clumps in a selected field one obtains typically a total area covered by clumps that is 1.4–3 times larger than the selected field. The clumps therefore cover the sky more or less completely and there are on average up to three clumps (with different velocities) along each line of sight. Due to the larger number of small clumps, beam dilution has to be taken into account. This increases somewhat the average number of clumps sensed in each telescope beam.

iii) Mass Spectrum of the Clumps

From the fitted parameters, the velocity and area integrated $C^{18}O$ $J = 2 \rightarrow 1$ intensity was calculated and converted into the clump mass using the conversion factors from the optically

TABLE 2
FITTED CLUMP PARAMETERS

Number (1)	$\Delta\alpha$ (2)	$\Delta\delta$ (3)	v_0 (km s ⁻¹) (4)	a_0 (K) (5)	Δx_1 (6)	Δx_2 (7)	φ (8)	Δv (km s ⁻¹) (9)	dv/dr (km s ⁻¹) (10)	φ_0 (11)
1.....	-76"	38"	19.5	22.8	28"	42"	31°	2.6	0.049	10°
2.....	-39	-96	19.3	23.1	31	69	63	1.7	0.013	-42
3.....	-98	-33	18.2	23.1	60	67	55	3.2	0.010	31
4.....	-69	5	20.0	17.1	28	35	131	2.2	0.044	-177
5.....	-138	52	19.6	16.1	31	50	87	2.7	0.021	-59
6.....	-55	-41	21.4	16.4	22	45	54	2.1	0.029	-84
7.....	-166	-23	20.0	12.4	90	46	-30	2.8	0.020	-77
8.....	16	-90	22.5	13.0	40	23	-24	2.0	0.050	-71
9.....	-69	-40	19.5	12.0	17	41	58	1.7	0.039	84
10.....	-77	30	23.4	12.0	22	33	35	2.0	0.022	-32
11.....	-105	-22	20.6	10.7	25	32	81	1.7	0.004	-38
12.....	-136	-6	19.0	10.3	19	34	62	1.6	0.026	-126
13.....	-107	46	22.4	10.3	47	18	3	2.0	0.020	127
14.....	-53	29	19.0	10.3	13	23	77	1.5	0.068	43
15.....	-165	68	16.5	10.2	34	23	11	1.6	0.014	-108
16.....	-52	-74	18.5	9.3	13	28	83	1.1	0.040	-53
17.....	-137	-92	18.6	9.2	47	47	13	1.8	0.010	-4
18.....	-138	30	22.0	9.2	27	50	93	2.1	0.011	67
19.....	-167	60	21.5	9.3	24	49	85	2.4	0.060	69
20.....	-113	-67	20.0	8.3	38	23	9	1.8	0.025	166
21.....	-135	-135	19.0	7.9	33	62	54	1.0	0.031	-18
22.....	-89	44	18.5	7.8	13	15	79	1.0	0.018	7
23.....	-38	-128	18.5	7.9	14	40	40	0.8	0.023	-138
24.....	-137	22	18.0	8.3	20	30	100	1.9	0.031	-155
25.....	-52	15	19.5	7.8	13	13	116	0.9	0.018	161
26.....	-76	44	18.5	7.6	13	14	65	1.9	0.125	-12
27.....	-113	68	20.5	7.9	21	30	130	1.4	0.062	172
28.....	-104	8	20.5	7.8	19	31	111	2.4	0.030	165
29.....	-30	-60	20.5	7.9	19	19	-2	1.3	0.005	84
30.....	-22	-97	19.0	7.8	19	19	2	1.1	0.015	90
31.....	-75	15	18.5	7.6	33	14	14	1.6	0.083	179
32.....	-135	44	16.5	7.6	16	31	129	1.0	0.009	-172
33.....	-98	-52	22.0	6.8	25	16	28	1.4	0.034	-4
34.....	-129	-45	21.0	7.0	39	25	-17	1.9	0.024	-22
35.....	-22	-83	26.5	7.8	13	13	98	0.5	0.048	59
36.....	-82	-15	16.0	7.0	16	24	53	1.4	0.042	96
37.....	-106	-127	21.0	7.2	46	26	13	2.1	0.019	127
38.....	-166	0	22.0	6.9	23	30	121	2.0	0.025	138
39.....	-90	45	21.0	6.3	15	16	157	1.0	0.024	105
40.....	-74	-23	18.0	6.6	15	25	102	1.4	0.037	-90
41.....	-136	45	24.0	7.0	21	29	140	1.3	0.026	-86
42.....	-120	-105	16.0	6.8	16	39	97	1.5	0.005	151
43.....	-89	22	16.5	6.6	21	31	109	2.1	0.039	133
44.....	-68	-150	17.5	6.3	79	44	68	1.6	0.012	133
45.....	-67	-52	18.0	6.2	17	18	56	0.9	0.009	-2
46.....	-31	-91	21.5	6.2	18	36	32	1.2	0.019	79
47.....	-68	8	21.5	6.1	22	34	25	1.2	0.006	121
48.....	-83	60	19.5	5.8	13	18	57	1.0	0.014	-53
49.....	-120	45	21.0	5.6	17	14	4	0.9	0.017	-95
50.....	-165	68	19.0	6.1	27	44	103	2.0	0.024	164
51.....	-98	-15	21.5	5.8	18	25	59	2.0	0.011	145
52.....	-67	37	13.5	6.3	24	19	-19	1.5	0.039	166
53.....	-37	-143	19.0	5.8	14	19	41	1.4	0.070	-21
54.....	-37	-127	23.0	5.9	13	15	94	0.7	0.009	-138
55.....	-105	-60	16.0	5.9	16	15	-12	1.4	0.016	-98
56.....	-165	-104	19.0	5.6	43	28	-33	2.2	0.043	-55
57.....	-60	38	20.5	5.9	15	27	34	1.4	0.013	167
58.....	15	-105	24.5	6.1	21	17	-17	1.3	0.029	-74
59.....	-120	60	22.0	5.5	18	14	34	0.6	0.025	149
60.....	-135	-104	22.0	5.6	24	40	93	1.3	0.007	101
61.....	-151	-15	18.0	5.6	21	65	79	1.5	0.008	137
62.....	-75	15	22.5	5.5	21	18	27	0.9	0.002	9
63.....	-120	-135	20.0	5.1	20	19	27	0.8	0.016	77
64.....	-158	16	19.5	5.6	19	35	26	1.9	0.034	-121
65.....	15	-105	21.5	5.6	16	27	113	2.1	0.044	-45
66.....	-75	-45	19.5	4.9	14	15	23	1.2	0.050	87
67.....	-60	-45	22.0	5.4	15	22	75	1.0	0.020	-80
68.....	-83	45	21.5	5.1	16	16	-1	0.8	0.008	106
69.....	-68	-151	16.0	5.2	87	13	15	1.3	0.017	142
70.....	-53	-82	17.0	5.1	21	15	-24	1.0	0.046	-72

TABLE 2—*Continued*

Number (1)	$\Delta\alpha$ (2)	$\Delta\delta$ (3)	v_0 (km s ⁻¹) (4)	a_0 (K) (5)	Δx_1 (6)	Δx_2 (7)	ϕ (8)	Δv (km s ⁻¹) (9)	dv/dr (km s ⁻¹) (10)	ϕ_v (11)
71.....	-75	-82	21.0	5.2	37	19	-9	1.5	0.006	-55
72.....	-75	-105	18.0	5.1	40	17	-12	1.5	0.042	124
73.....	-120	-15	18.5	5.1	19	35	118	0.9	0.028	-120
74.....	-67	-22	17.5	5.1	13	24	3	1.0	0.068	-105
75.....	-68	-150	23.0	5.2	26	15	10	0.7	0.069	180
76.....	-75	30	17.0	4.9	16	19	73	1.0	0.017	22
77.....	-98	23	23.0	5.1	20	13	20	2.5	0.106	-27
78.....	-68	-150	27.5	5.4	22	13	1	0.6	0.025	-12
79.....	-128	-38	23.0	5.2	36	30	3	1.4	0.022	-70
80.....	-98	-8	16.5	4.9	13	17	70	2.0	0.097	13
81.....	-52	-60	18.0	4.9	14	30	98	0.7	0.020	30
82.....	-105	45	24.0	5.1	13	20	69	1.5	0.071	-168
83.....	-45	-15	21.0	4.9	17	19	71	0.8	0.007	-80
84.....	-120	-60	18.0	5.2	28	13	30	1.8	0.035	128
85.....	-30	-75	19.0	4.8	20	18	28	0.9	0.009	-38
86.....	-53	-53	19.5	4.9	17	21	154	2.0	0.044	108
87.....	-97	-38	21.5	4.7	19	17	-22	1.0	0.020	21
88.....	-38	-97	17.5	4.8	22	17	-29	0.8	0.006	-138
89.....	-165	-90	21.5	5.1	31	74	117	1.8	0.007	74
90.....	-83	15	20.5	4.7	15	15	74	1.4	0.025	-47
91.....	-150	0	23.5	4.7	17	18	103	1.0	0.017	110
92.....	-113	-83	20.5	4.9	15	30	150	1.7	0.018	-146
93.....	-120	-135	15.5	4.7	17	25	140	1.2	0.026	-33
94.....	-165	-90	17.5	4.9	26	36	125	1.1	0.026	45
95.....	120	45	18.5	4.5	27	13	-2	1.2	0.021	108
96.....	105	-120	19.0	4.8	27	37	129	1.5	0.040	-30
97.....	-23	30	21.5	4.8	13	32	63	0.5	0.049	119
98.....	-23	-143	20.0	4.5	13	35	55	1.0	0.055	142
99.....	-90	45	20.0	4.2	13	19	95	1.1	0.006	-179
100.....	-165	-60	19.5	4.5	17	38	72	0.9	0.018	-168
101.....	-120	-15	21.5	4.5	15	29	46	1.6	0.015	-85
102.....	-38	-98	21.0	4.2	17	14	-1	1.0	0.012	-10
103.....	-75	-23	21.0	4.4	16	18	124	1.0	0.023	99
104.....	-165	-23	21.5	4.7	21	39	30	1.8	0.008	-90
105.....	-97	-15	23.0	4.5	13	19	93	1.0	0.025	109
106.....	-38	-53	17.0	4.8	13	35	101	1.0	0.039	-88
107.....	-165	30	20.0	4.2	15	19	109	0.9	0.006	-179
108.....	-53	30	14.0	4.4	13	17	116	1.3	0.016	134
109.....	-53	-68	21.5	4.1	17	17	73	1.0	0.015	160
110.....	-60	0	19.5	4.2	26	15	3	1.2	0.058	-123
111.....	-150	60	21.0	3.9	14	16	119	1.2	0.025	156
112.....	-68	-150	20.0	3.9	16	23	118	0.9	0.020	80
113.....	-90	-30	17.0	4.2	17	24	82	1.0	0.036	58
114.....	-105	7	18.0	3.9	16	17	62	1.2	0.015	-59
115.....	-23	-143	24.5	4.2	14	15	76	0.8	0.002	150
116.....	-83	-15	14.0	4.2	17	19	118	1.1	0.017	70
117.....	-90	68	20.0	3.9	14	18	112	1.1	0.003	-124
118.....	-53	-98	20.5	3.9	16	21	89	1.0	0.019	-156
119.....	-83	-83	22.5	4.1	18	17	4	0.8	0.004	40
120.....	-90	45	17.5	4.2	32	22	44	1.6	0.041	179
121.....	-150	-120	18.5	3.9	17	21	59	0.8	0.008	19
122.....	-112	-97	14.5	4.1	19	17	-10	0.7	0.013	-50
123.....	-150	-45	14.5	4.1	18	17	-15	0.8	0.008	141
124.....	-60	-150	22.0	3.9	21	17	-18	0.7	0.015	-38
125.....	0	-68	22.0	3.9	13	27	98	1.0	0.043	-89
126.....	-98	30	21.5	3.8	16	20	56	1.0	0.009	-30
127.....	-113	-143	22.0	4.1	30	13	3	2.1	0.160	-179
128.....	-105	45	25.5	4.1	24	13	-1	1.1	0.048	165
129.....	-22	-112	17.0	3.8	14	15	158	1.7	0.114	-80
130.....	-52	30	17.0	3.9	32	13	-23	1.7	0.068	-142
131.....	-15	-135	18.5	3.7	14	26	117	0.7	0.004	170
132.....	-158	23	16.5	4.4	47	32	23	1.5	0.014	158
133.....	-38	-97	22.0	3.9	15	39	151	1.5	0.008	-48
134.....	-38	-38	21.5	3.8	15	21	80	1.0	0.006	-113
135.....	-135	0	22.5	3.7	20	21	123	0.8	0.008	-52
136.....	-98	8	24.0	3.8	17	17	95	1.0	0.020	-103
137.....	-90	-90	18.0	3.7	35	14	-28	0.6	0.024	-85
138.....	-53	45	21.0	3.7	15	13	4	1.0	0.050	107
139.....	-157	60	23.0	3.8	19	67	75	1.2	0.004	-112
140.....	-38	-90	14.5	3.9	16	19	63	1.0	0.017	-141
141.....	-105	0	19.5	3.9	28	38	107	1.1	0.038	69

TABLE 2—*Continued*

Number (1)	$\Delta\alpha$ (2)	$\Delta\delta$ (3)	v_0 (km s ⁻¹) (4)	a_0 (K) (5)	Δx_1 (6)	Δx_2 (7)	ϕ (8)	Δv (km s ⁻¹) (9)	dv/dr (km s ⁻¹) (10)	ϕ_v (11)
142.....	-45	-68	23.5	3.8	14	26	85	1.4	0.030	66
143.....	-113	-8	24.5	3.8	16	15	18	0.7	0.026	-14
144.....	-165	60	17.5	3.8	31	15	-12	1.0	0.061	50
145.....	-60	-120	18.5	3.5	16	22	124	1.1	0.010	-134
146.....	-68	-150	18.5	3.7	13	37	106	0.6	0.038	-10
147.....	-30	-15	24.0	3.9	25	31	99	0.6	0.025	-151
148.....	-165	-23	17.5	3.5	17	18	56	1.0	0.016	78
149.....	-52	15	20.5	3.8	13	31	47	1.1	0.055	166
150.....	-53	-68	14.0	3.8	14	19	66	0.8	0.014	160
151.....	-45	-120	21.0	3.5	19	18	-31	0.9	0.017	-35
152.....	-113	-143	14.5	4.1	30	42	149	1.4	0.012	-9
153.....	-105	-143	19.0	3.4	20	16	34	0.8	0.025	180
154.....	-60	38	12.5	3.7	50	13	39	0.6	0.031	13
155.....	-30	-45	20.0	3.5	19	21	123	0.9	0.011	-138
156.....	-52	-83	15.5	3.7	16	15	19	0.8	0.041	-58
157.....	-45	30	15.0	3.7	20	17	12	0.9	0.018	-54
158.....	-60	45	19.0	3.4	14	16	49	0.9	0.013	135
159.....	-75	-45	18.5	3.4	15	17	108	0.9	0.018	161
160.....	-128	68	20.0	3.2	13	30	137	1.4	0.084	-81
161.....	-60	-82	18.5	3.5	16	15	-22	0.7	0.040	126
162.....	-38	-98	24.0	3.5	17	17	57	1.0	0.014	-67
163.....	-60	-45	20.5	3.4	19	20	124	0.9	0.007	157
164.....	-30	0	19.5	3.5	13	17	50	1.7	0.016	132
165.....	-82	-143	21.0	3.4	16	16	124	1.0	0.015	118
166.....	-38	-143	20.0	3.4	17	18	56	0.9	0.010	-110
167.....	0	-90	21.0	3.2	16	20	56	0.9	0.004	-95
168.....	0	-68	18.5	3.5	17	35	83	0.9	0.015	160
169.....	-38	-128	13.5	3.4	13	15	76	1.1	0.035	-132
170.....	-68	45	21.5	3.4	13	34	89	0.7	0.033	-155
171.....	-105	-90	15.5	3.5	16	21	124	0.9	0.006	-66
172.....	-82	8	17.5	3.5	13	33	109	1.1	0.037	87
173.....	-23	-142	22.0	3.2	14	17	114	0.9	0.024	63
174.....	-105	-127	17.5	3.8	38	32	-11	1.5	0.017	124
175.....	-98	-68	20.0	3.2	18	24	90	0.8	0.057	-13
176.....	-112	23	14.5	3.7	38	27	-4	0.6	0.023	129
177.....	-45	-135	16.5	3.2	17	24	79	1.0	0.020	33
178.....	-120	45	20.0	3.2	17	13	3	1.2	0.062	-34
179.....	-113	-68	22.0	3.5	30	38	152	1.3	0.014	-48

Col. (1): clump number. Cols. (2) and (3) clump center position. Col. (4): clump center velocity. Col. (5): clump peak intensity. Cols. (6)–(7) clump spatial FWHM along the two principal axes. Col. (8): orientation of the first principal axis (counterclockwise from west). Col. (9): clump velocity FWHM. Col. (10): clump internal velocity gradient. Col. (11): direction of internal velocity gradient (counterclockwise from west).

thin, thermalized approximation at $T_{\text{kin}} = 50$ K (with a $\text{C}^{18}\text{O}/^{12}\text{CO}$ isotopic abundance of 1/500 and a CO/H_2 abundance of 8×10^{-5}):

$$M = T_0(\text{K}) \times \Delta x'' \times \Delta y'' \times \Delta v (\text{km s}^{-1}) \times 9.76 \times 10^{-3} M_{\odot}.$$

As discussed above, the effects of subthermal excitation in higher levels and slight optical depth in the $2 \rightarrow 1$ transition almost cancel, so that the actual clump mass will be not too much different from this estimate, independent of the exact temperature and density of the individual clump.

The resulting clump mass distribution (Fig. 11) is consistent with a power-law distribution

$$dN/dM \propto M^{-\alpha}, \quad \text{with } \alpha = 1.72 \pm 0.15. \quad (1)$$

The exponent was determined by a least-squares fit to the mass distribution taking into account the $(\Delta N)^{1/2}$ statistical errors in the distribution. Over the mass range $10 < M/M_{\odot} < 10^3$, the spectrum is well-fitted by a single power law. In particular, there is no evidence for a preferred size or mass scale of the clumps, similar to the one reported for cool giant molecular

clouds, where according to Falgarone and Péroult (1987) the basic building blocks are of 1–3 pc size and a few $100 M_{\odot}$ mass. The Jeans mass for the typical physical parameters of the emitting gas in M17 SW ($T \approx 50$ K, $n \approx 10^{5.2} \text{ cm}^{-3}$) is about $10 M_{\odot}$, close to the lower limit of clump masses given by the limited resolution and sensitivity of the observations. It is thus not clear, whether the turnover from the power law at $10 M_{\odot}$ in the lowest mass bin reflects the influence of the Jeans mass as a physical lower limit to the mass spectrum, or whether it is just due to the incompleteness of the sample.

Note that with a power-law index $\alpha = 1.7$, the most massive clumps contribute most to the mass of the complex. A similar power-law spectrum, with an exponent $\alpha = 1.5$, has been found in the case of the Rosette Nebula (Blitz 1987), where about 80 individual clumps with a comparable range of mass ($18\text{--}2800 M_{\odot}$) have been identified. On the other hand, Loren (1989a) derives an exponent $\alpha = 1.1$ in his study of the ρ Ophiuchus complex. Interestingly, and pointing toward a common fragmentation scenario, a quite comparable mass spectrum has been reported for samples of giant molecular clouds ($\alpha \approx 1.4\text{--}1.6$ for $400 < M/M_{\odot} < 2 \times 10^5$: Casoli, Combes, and Gérin 1984; $\alpha \approx 1.6$ for $10^4 < M/M_{\odot} < 10^6$: Sanders, Scoville, and

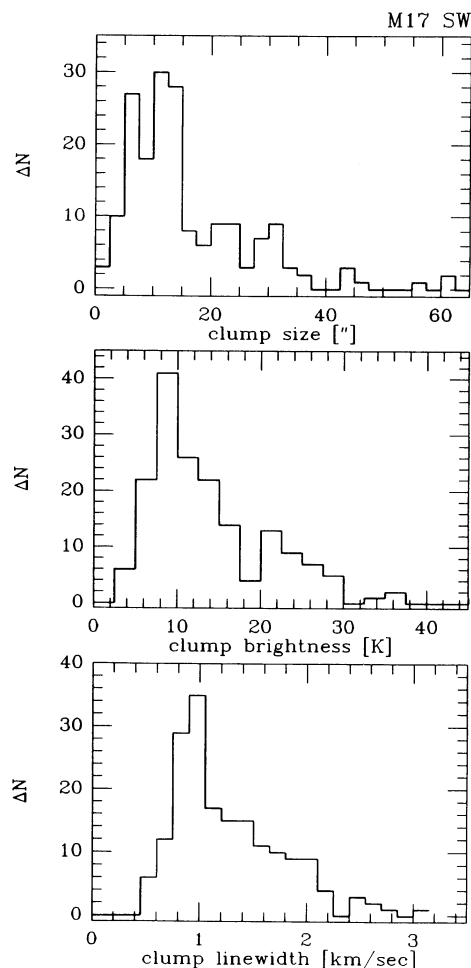


FIG. 10.—With the clump fitting procedure described in the Appendix, the M17 SW molecular cloud (as seen in the $\text{C}^{18}\text{O } J=2 \rightarrow 1$ line) was decomposed into 179 individual clumps. Major characteristics of these clumps, namely their distribution of size (deconvolved from the beam size), intrinsic brightness, and line width, are displayed. For a discussion on the reliable parts of these distributions, see § IVb.

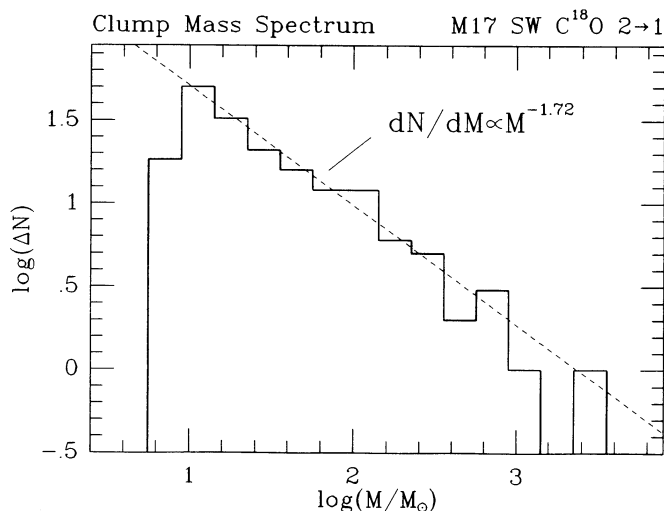


FIG. 11.—Mass spectrum of the clumps into which the $\text{C}^{18}\text{O } J=2 \rightarrow 1$ emission from the M17 SW molecular cloud has been decomposed. The distribution is well fitted by a power law $dN/dM \propto M^{-\alpha}$ with $\alpha = 1.72 \pm 0.15$.

Solomon 1985; see also Scalo 1985), and also for H I clouds ($\alpha = 1.75$, $10^3 < M/M_\odot < 10^6$; Perry and Helfer 1972; $\alpha \approx 1.9$ – 2.1 , $0.1 < M/M_\odot < 500$; Dickey and Garwood 1989).

A power-law spectrum with a power close to -1.5 for the mass distribution of clumps is predicted if the clumps represent a steady state equilibrium between coagulation of individual clumps and fragmentation of the resulting, higher mass clumps, e.g., when they start to collapse under their own gravitational force (Field and Saslaw 1965; Nakano 1984; Spitzer 1982). Although the models resulting in a spectrum with a power-law index $\alpha = 1.5$ are based on specific assumptions about the coalescence cross section and the way mass is fed back into lighter clumps by fragmentation of the bigger clumps, the mass spectrum for any steady state equilibrium will be very similar, not very sensitively depending on the details of the individual coagulation and fragmentation processes (Field and Hutchins 1968; Taff and Savedoff 1972, 1973; Arny and Weissman 1973; Silk and Takahashi 1979).

The clump mass spectrum derived here emphasizes the importance of the underlying fragmentation process in the parent cloud on the resulting initial mass function of the newly formed stars. Although the way in which the clump mass spectrum translates into the stellar mass spectrum is barely known, the latter seems to be defined by both the physical evolution of the molecular cloud and details of the later stages in the accretion process. With the assumption that the relation between the initial clump mass M_{cl} and the final stellar mass M_* forming out of this clumps is $M_* = \epsilon M_{cl}^p$ ($p < 1$), where p is close to 0.5, a clump mass spectrum of the form (1) yields a stellar IMF $\propto M^{-x}$, where $x = (\alpha + p - 1)/p$ (Zinnecker 1989). With $p = 0.5$ and $\alpha = 1.7$ from the mass spectrum fitted to the M17 SW clumps, we obtain $x = 2.4$, very close to the Salpeter IMF ($x = 2.35$). For the range of higher masses ($M > 9 M_\odot$), relevant for most of the mass range covered by the observed M17 SW clump spectrum, the index of $p = 0.5$ is an approximation to model calculations by different authors (Yorke 1979; Tutkov and Shustov 1981) and results mostly from the higher efficiency for higher mass fragments of expelling the outer layers of the collapsing clump by radiation pressure, stellar winds, or ionization fronts. For lower mass stars, the $p = 0.5$ power law is rather speculative but may result for magnetic field-limited accretion governed by ambipolar diffusion, where the outer portions of a collapsing fragment are retained from falling in by the embedded magnetic field (Nakano 1984; see, however, Lizano and Shu 1988).

iv) Virialization of Individual Clumps

With the mass, size, and line width of individual clumps determined, we can check whether the individual clumps satisfy the criterion for virial equilibrium: $(\ln 2/2\pi)^{1/2} GM/R = 3 \Delta v^2/8 \ln 2$ (the numerical factor on the left-hand side is that for the potential energy of a clump with Gaussian density distribution, R is the HWHM). Figure 12 shows that the fitted clumps all fall with their measured line width close to the relation predicted by virial equilibrium.

The range of clump sizes and line widths covered by the present observations, about one order of magnitude, is insufficient to verify the correlation between line widths and sizes of individual clumps, $\Delta v \propto R^{0.4}$ – $R^{0.5}$, given by Larson (1981) (Fig. 13a). Larson's mass-size relation, $M \propto R^2$, however, is satisfied reasonably well (Fig. 13b). Although a plot of M versus R is to some extent influenced by the fact that the mass is calculated as the product of column density $\times R^2$ and the observations prefer a certain column density range, the corre-

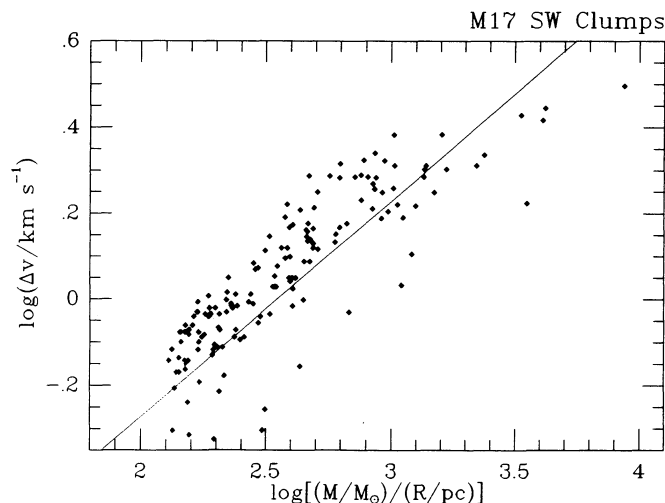


FIG. 12.—Mass vs. line width of the M17 SW clumps. Almost all the clumps lay above, but close to the relation predicted for virialized clumps with a Gaussian density distribution $\Delta v^2 = 4 \ln 2/3 (2 \ln 2/\pi)^{1/2} GM/(D/2)$, where D is the FWHM of the clump. The clump line width has been corrected for the small contribution of the thermal width, 0.27 km s^{-1} at $T_{\text{kin}} = 50 \text{ K}$.

lation in Figure 13b is actually more significant because the range of clump column densities (i.e., peak temperature \times line width) observed is definitely broader than an order of magnitude, whereas the scatter in the correlation in Figure 13b is definitely smaller than a factor of 10. The correlations are thus similar to the ones found by Loren (1989a, b) in his $^{13}\text{CO } J = 1 \rightarrow 0$ study of the ρ Ophiuchus complex.

v) Clump Densities

If we assume an extension along the line of sight of each clump equal to the geometric mean of the two fitted principal axes in the plane of the sky, we can also calculate the peak

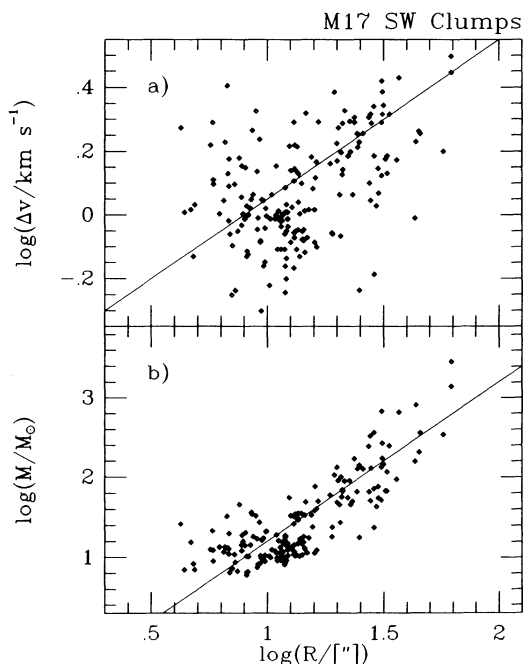


FIG. 13.—The distribution of clump masses vs. size and clump line widths vs. size for the M17 SW clumps. The straight lines correspond to the empirical laws $\Delta v \propto R^{0.5}$, and $M \propto R^2$.

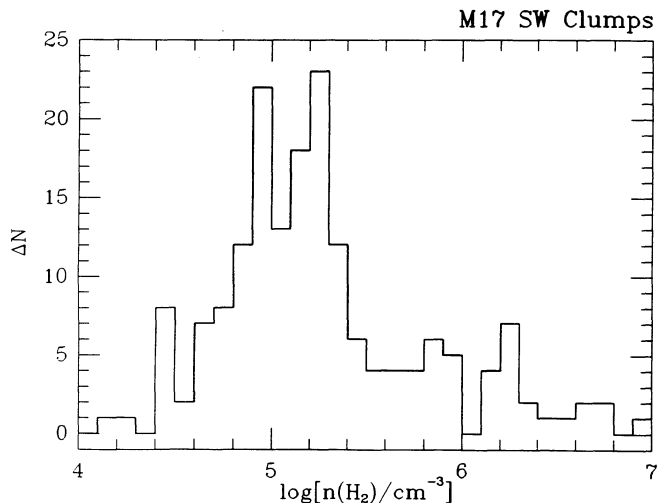


FIG. 14.—Volume density spectrum of the M17 SW clumps, as derived from the C^{18}O column density and the size of individual clumps.

density of each clump (from the velocity integrated intensity, i.e., column density, divided by the line of sight extent). The resulting distribution of peak densities is plotted in Figure 14. Most of the clumps have densities between 10^5 cm^{-3} and a few times 10^5 cm^{-3} . It is important to note, that the bulk of the gas traced by the $\text{C}^{18}\text{O } J = 2 \rightarrow 1$ line in the M17 SW cloud core has densities of 10^5 cm^{-3} or higher, two orders of magnitude higher than the critical density of the $\text{C}^{18}\text{O } J = 2 \rightarrow 1$ transition of only a few times 10^3 cm^{-3} . This emphasizes that the critical density of a transition observed in strong emission only gives a *lower limit* to the density in the emission region.

The average density in the clumps visible in C^{18}O is high, but still by a factor of 3–10 lower than the density required for the isotopic C^{34}S emission as discussed above. This is another strong evidence for density structure within the clumps, as was already indicated by the inconsistent results obtained when trying to explain the main isotopic CS emission as coming from the same material as the isotopic C^{34}S emission.

vi) Volume Filling Factor

If we take as the equivalent volume of each Gaussian-shaped clump the volume a homogeneous clump with the same total mass would have, i.e., $V_{\text{clump}} = (\pi/4 \ln 2)^{3/2} \Delta \xi_1 \times \Delta \xi_2 \times \Delta \xi_3$, where $\Delta \xi_1$, $\Delta \xi_2$ are the fitted FWHM in the plane of the sky corrected for the beam size, and $\Delta \xi_3 = (\Delta \xi_1 \times \Delta \xi_2)^{1/2}$, as discussed above, we can compare the volume filled by the fitted clumps compared to the total volume observed. Here we again assume that the line of sight extent of the M17 cloud core is 3'.3, similar to the observed extent along the H II region/molecular cloud interface. Including most of the region observed in $\text{C}^{18}\text{O } 2 \rightarrow 1$ ($\Delta \alpha = -165''$ to $-30''$, $\Delta \delta = -135''$ to $75''$), this gives a volume filling factor for all clumps of 31%. Selected subsections of the cloud, like (a) the area around the northern condensation ($\Delta \alpha = -105''$ to $-57''.5$, $\Delta \delta = 7''.5$ to $60''$), (b) the central region ($\Delta \alpha = -120''$ to $-50''$, $\Delta \delta = -55''$ to $-5''$), and (c) the southern ridge along the H II region interface ($\Delta \alpha = -60''$ to $-30''$, $\Delta \delta = -112''.5$ to $-50''$) have similar volume filling factors (29%, 41%, and 26%, respectively), if the line-of-sight extent for the whole cloud is taken as the total reference volume. This may be reasonable for the central region and the southern ridge. It likely overestimates the line-of-sight extent for the northern condensation. If we assume

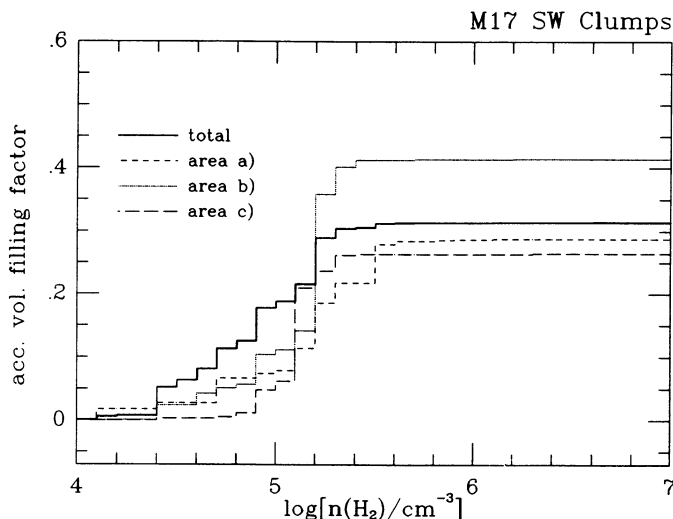


FIG. 15.—Accumulative volume filling factor of the M17 SW clumps for the total area observed in $C^{18}O$ and three subsections as defined in the text.

that the northern condensation is roughly spherical (i.e., has a line-of-sight extent similar to its size in the plane of the sky, about $1'$), its volume filling factor gets corrected upward to about 90%.

The volume filling factors quoted so far include all $C^{18}O$ emission. The volume filling factor of higher density gas is smaller. Figure 15 shows the fraction of the total volume filled by clumps, versus the peak density of the clumps in the four cases defined above: for the whole cloud, for the northern condensation, for the center region, and for the ridge. In the case of the whole cloud, the distribution rises smoothly between densities of $10^{4.4}$ and $10^{5.4} \text{ cm}^{-3}$. The volume filling factor of clumps with peak densities greater than $10^{5.0} \text{ cm}^{-3}$ is only 13%. For the selected, smaller core regions, the distribution shows less than about 5% of the volume filled by clumps with densities below $10^{5.0} \text{ cm}^{-3}$ and then a very sharp rise within a factor of about 5 in density to the total volume filling factor.

The fact that essentially all the observed $C^{18}O$ $2 \rightarrow 1$ emission can be attributed to clumps that fill only about 30% of the total volume allows an estimate of the clump to interclump density contrast. Assuming roughly equal excitation conditions for the clump and interclump gas, the observed intensity in a given, optically thin line (like $C^{18}O$ $J = 2 \rightarrow 1$) is given by the column density ratio of the clump and interclump medium. With the volume filling factor ϕ_v , the H_2 density in the clumps n_c , and in the interclump medium n_{ic} , this gives for the intensity ratio $I_c/I_{ic} = \phi_v/(1 - \phi_v) \times n_c/n_{ic}$. To obtain a conservative limit, we assume that confusion in attributing the observed emission to individual clumps rather than to an underlying, smoother level of emission from the interclump gas, starts at the 10% level of the intensity, i.e., $I_c/I_{ic} \geq 10$. With $\phi = 0.3$, this gives a clump to interclump density contrast n_c/n_{ic} of at least 23. About 10% of the molecular material could thus be homogeneously distributed at a density of several 10^3 cm^{-3} . This lower density interclump gas, if at a temperature of about 120–150 K, may be responsible for the bright, wide line emission seen in the low- J , high-resolution ^{12}CO spectra (Fig. 5).

The above argument assumes that the excitation conditions are similar for the clump and interclump gas, which is certainly not a very good assumption. The observations of $[C \text{ II}]$ $158 \mu\text{m}$

fine-structure line emission and high- J CO emission from very warm molecular gas (Harris *et al.* 1987; Stutzki *et al.* 1988) indicate that yet another, substantial fraction of the material is localized in warm (200–400 K), dense ($\approx 10^{4.5} \text{ cm}^{-3}$) photo-dissociation regions. This emission component seems to have a filling factor less than unity (≈ 0.3) and shows line widths, at least in the CO $J = 7 \rightarrow 6$ line, comparable to the bulk of the material (traced by $C^{18}O$ $J = 2 \rightarrow 1$), and significantly smaller than seen in the bright emission from low- J ^{12}CO lines. A consistent interpretation of the cloud core structure clearly needs future, high-angular resolution studies of the different ionized, atomic, and molecular gas components.

vii) Comments

One may argue that the results given above, based on the decomposition of the observed intensity distribution into Gaussian-shaped clumps, have to be considered with some caution. As an example, it is not clear to what extent the derived mass spectrum of the clumps depends on the assumed Gaussian shape of the clumps. If, for example, the actual clumps are somewhat more extended with a sharper drop-off than Gaussian (this could, e.g., result from substantial optical depth in clumps with Gaussian density distribution), the Gaussian fitting procedure would tend to fit a central clump and several smaller clumps along the clump perimeter, thus artificially introducing several low-mass clumps for each big clump. Similarly, if the small-scale spatial distribution is more filamentary, rather than clumpy, the Gaussian fitting procedure would tend to fit several separate clumps to each elongated filamentary structure. As described in the Appendix, we tested the behavior of the decomposition procedure for the case of circular, constant-surface brightness clumps. Indeed, a tail of lower mass clumps is found in the decomposed mass spectrum, but the power-law index in the central portion of the mass spectrum is not severely altered.

Although the length scale corresponding to the $13''$ beam size of the IRAM 30 m telescope at 230 GHz is close to the Jeans length for the average physical parameters of the clumpy gas in M17, the source may still be partially unresolved. Many of the observed structures may break up into even smaller clumps once observed with even higher angular resolution. On the other hand, the good agreement of the fitted clump parameters to the relation imposed by virial equilibrium may be taken as an indication that the fitted clumps represent substructure with physical relevance. Also, quantities like the volume filling factor should still be represented well by the Gaussian decomposition, even if the shape of individual clumps is not really Gaussian. On the other hand, the derived volume filling factor depends sensitively on the assumed line-of-sight extent of the clumps and the total source.

c) The Northern Condensation: An Expanding Cavity?

The region slightly west of the radio continuum arc discovered by Felli, Churchwell, and Massi (1984) draws special attention for several reasons. It is the area of peak emission both in the $C^{18}O$ $2 \rightarrow 1$ and the isotopic CS lines. The distribution of the molecular emission follows very closely the arc-shaped radio continuum feature (Fig. 16), confirming the earlier suspicion that we observe an edge on, very sharp molecular cloud/ $H \text{ II}$ region interface. The molecular emission shows a very striking velocity structure (see below, and Fig. 17). The region also contains several embedded sources indicative of very recent star-forming activity. The extremely young, ultra-

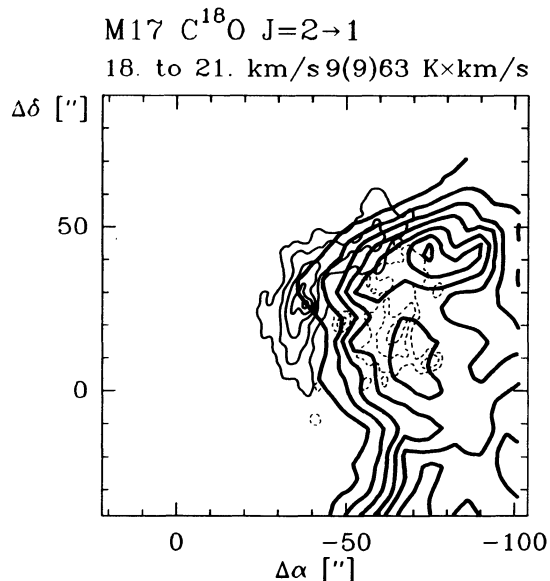


FIG. 16.—The region of the northern condensation close to the radio continuum arc discovered by Felli, Churchwell, and Massi (1984) (*thin solid contours*). *Heavy solid contours*: $\text{C}^{18}\text{O } J=2 \rightarrow 1$ emission integrated from 18–21 km s^{-1} in 9 K km s^{-1} contours. *Thin dashed contours*: the $\text{NH}_3(J, K) = (1, 1)$ integrated intensity contours from Massi, Churchwell, and Felli (1988). Note the half-circular, shell-like appearance of the $\text{C}^{18}\text{O } 2 \rightarrow 1$ emission enclosed by the radio continuum arc.

compact H II region UCL, coincident with the $10.6 \mu\text{m}$ source detected by Harper *et al.* (1976), three H_2O maser features and at least one early-type star (Number 92 from Chini, Elässser, and Neckel 1980) are located in the region. The NH_3 observations by Güsten and Fiebig (1988) show very high temperatures, possibly greater than 200 K, in this region. Massi, Churchwell, and Felli (1988) identify several ammonia clumps from their interferometric observations with the VLA.

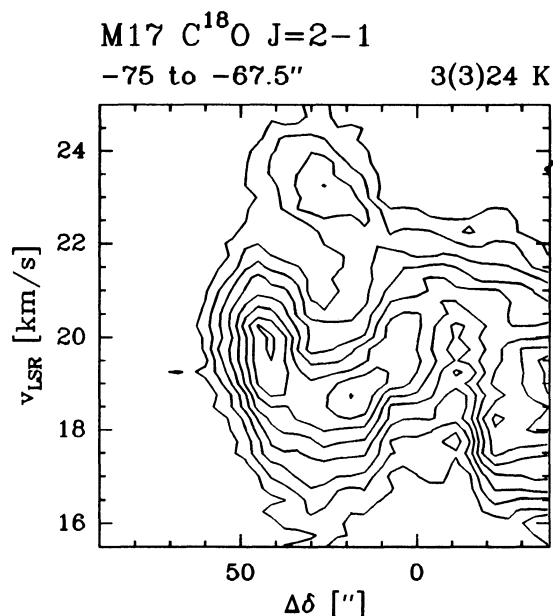


FIG. 17.—Velocity-declination cut across a central strip through the northern condensation ($-75'' < \Delta\alpha < -67.5''$).

We fully sampled this $1'$ by $1'$ region in our $\text{C}^{18}\text{O } 2 \rightarrow 1$ map. The clump decomposition procedure described above identified 23 clumps with a total mass of $1500 M_\odot$. Comparison between the NH_3 clumps identified by Massi, Churchwell, and Felli (1988) and the $\text{C}^{18}\text{O } 2 \rightarrow 1$ velocity channel maps shows no similarity (Fig. 18). This may not be too surprising, since the interferometer maps contain only about 15% of the total $\text{NH}_3(1, 1)$ flux measured with the single dish (Güsten and Fiebig 1988). All the structure visible in the NH_3 interferometer map is located in regions of strong gradients in the single-dish C^{18}O map. This may perhaps indicate that the interferometer detected only regions with strong changes in the NH_3 intensity.

The spatial structure visible in the $\text{C}^{18}\text{O } 2 \rightarrow 1$ emission (Fig. 16) looks like half a spherical shell directly enclosed by the radio continuum arc. The shell with a diameter of 0.35 pc is open toward the west, where the C^{18}O map shows a hole in the molecular cloud that is actually filled by radio continuum emission (see Fig. 1). The declination-velocity maps across this feature at different right ascensions show a striking, half-circular structure (Fig. 17). This feature may be interpreted as expansion of a shell at a velocity of 1.5 km s^{-1} . The other side of the shell, the one with velocities pointing away from the observer, is missing. If the shell is expanding, the missing side would be the back side of the shell. Alternatively, the shell could collapse and the front side would be missing. Either way, the fact that the shell is not only open to the west but also to either the front or back side, fits with the spatial arc-like appearance. A full spherical shell would have a lower contrast between the rim and the center positions. The fact that no embedded sources are visible, and that there is thus a large amount of absorbing material along the line of sight toward the observer, favors the explanation as an expanding rather than collapsing, shell.

The mass contributed by the clumps with center velocities in the range 18–21 km s^{-1} (the range of the shell-like feature in the position velocity diagram, Fig. 17) is about $10^3 M_\odot$. If the

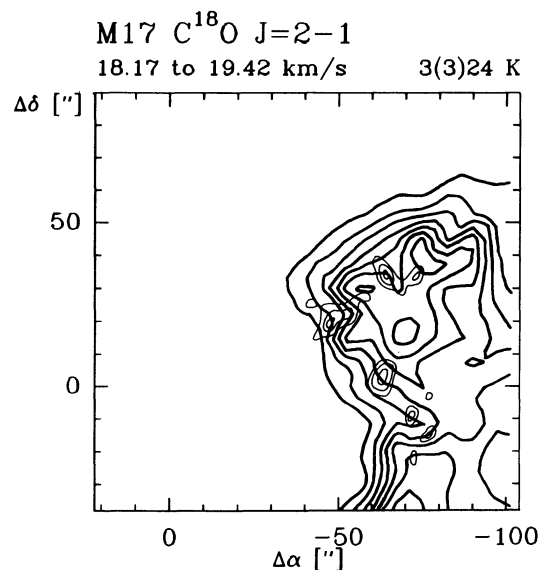


FIG. 18.—Overlay of the $\text{C}^{18}\text{O } J=2 \rightarrow 1$ IRAM 30 m (this paper) and $\text{NH}_3(J, K) = (1, 1)$ (VLA; Massi, Churchwell, and Felli 1988) map in the velocity interval 18.17–19.42 km s^{-1} . The interferometer seems to emphasize structure near the steepest gradients visible in the single-dish C^{18}O data.

structure is an expanding shell with an expansion velocity of about 1.5 km s^{-1} , then its mechanical momentum is $1.5 \times 10^3 M_{\odot} \text{ km s}^{-1}$, and its kinetic energy is about 10^{46} ergs. The expansion motion thus requires a mechanical energy input of at least $10^5 L_{\odot} \text{ yr}$. Energy loss in the interaction of an outflow with the ambient material will push this value up. The ratio of radius and expansion velocity gives a kinematical age of $\approx 10^5$ yr, which is an upper limit, because not all the material will have had to move out from the central source and the velocity may have been larger earlier on, being slowed down by the swept-up material. The mechanical energy input required to create the present structure is then at least around a few L_{\odot} . Assuming a wind velocity of 100 km s^{-1} , a momentum flow of $0.015 M_{\odot} \text{ yr}^{-1} \text{ km s}^{-1}$ is needed to drive the expansion. Both the momentum and the energy are well within the range of values spanned by typical outflow sources. Therefore, one or a few outflows from low- to medium-mass embedded objects can easily account for this mechanical luminosity. No source able to provide this energy input is known close to the center of the structure at about $\alpha_{50} = 18^{\text{h}}17^{\text{m}}28^{\text{s}}.3$, $\delta_{50} = -16^{\circ}13'00''$. The very high extinction toward this region, however, will make the detection of the active source(s) in this region very difficult.

V. SUMMARY

The high-angular resolution mapping of the M17 SW region in the $\text{C}^{18}\text{O } J=2 \rightarrow 1$ line, tracing the bulk of the molecular cloud material, has *directly* revealed the clumpy structure, both in the spatial and in the velocity domain, of an entire giant molecular cloud core. Clumps are identified down to sizes of 0.05 pc . The individual clumps have line widths as small as 0.5 km s^{-1} . The observations nicely confirm the picture of a macroturbulent cloud put forward by Martin, Sanders, and Hills (1984), and they confirm earlier indications of a clumpy structure of the cloud core (Snell *et al.* 1984). The close agreement between the $\text{C}^{18}\text{O } 2 \rightarrow 1$ map and isotopic C^{34}S maps suggests that the bulk of the material resides in clumps with densities typically a few times 10^5 cm^{-3} . The ^{34}CS excitation analysis indicates even higher densities, suggesting density structure within the clumps. The clumpy structure matches the one found in the radio continuum emission from the adjacent H II region, which Felli, Churchwell, and Massi (1984) interpreted as resulting from ionized surfaces of neutral, high-density clumps left over from the molecular cloud after the ionization front had progressed into the molecular material.

The small-scale clumpy structure implies that lower angular resolution observations are severely affected by beam dilution. This is nicely illustrated by our high-angular resolution ^{12}CO spectra toward selected positions: deep self-absorption notches and very high brightness temperatures in between imply that

the ^{12}CO emission is completely dominated by only a very small fraction of the total material with rather untypical conditions. In particular, the agreement between the ^{12}CO brightness temperatures of about 50 K , found in low-angular resolution observations, and the kinetic temperature of the bulk of the molecular gas, estimated from dust continuum observations of NH_3 lines, seems to be accidental.

The very bright ^{12}CO emission in between the deep self-absorption notches may indicate the presence of warm, low-density interclump gas ($T_{\text{kin}} \approx 150 \text{ K}$, $n(\text{H}_2) \approx \text{several } 10^3 \text{ cm}^{-3}$), in addition to the even warmer ($200\text{--}400 \text{ K}$), dense ($10^{4.5} \text{ cm}^{-3}$) gas traced in the $\text{CO } J=7 \rightarrow 6$ line originating in photodissociation surfaces of the dense clumps.

The decomposition of the observed $\text{C}^{18}\text{O } 2 \rightarrow 1$ emission into Gaussian shaped clumps identifies 179 individual clumps that account for all the observed C^{18}O emission. These clumps have masses ranging from a few to a few thousand M_{\odot} and densities ranging from $10^{4.5}\text{--}10^7 \text{ cm}^{-3}$, with only very few clumps at the extreme values of this density range. The mean density of the clumps is at $10^{5.4} \text{ cm}^{-3}$. The mass spectrum of the clumps follows a power law, $dN/dM \propto M^{-1.7}$. The masses, sizes, and velocity widths of individual clumps are all close to the relations representing virial equilibrium.

The volume filling factor of all clumps is about 30%, assuming a line-of-sight extent of the source equal to the extent in the plane of the sky along the H II region/molecular cloud interface. The volume filling factor is close to unity in the northern condensation, if one assumes a smaller extent along the line of sight, similar to its diameter on the sky. Based on the volume filling factor, we estimate a clump/interclump density contrast of at least 23.

Our results support the picture of the M17 SW cloud core suggested by Stutzki *et al.* (1988) in order to explain the large spatial extent of C II emission into the molecular cloud, requiring the presence of ionizing UV radiation deep inside the cloud: due to its clumpiness and small filling factor, the cloud core can be penetrated by the UV radiation much further than the average density of the cloud core suggests. The clump/interclump density contrast, however, has to be much larger than the lower limit derived here, in order to allow UV penetration depths as deep as necessary to explain the large C II emission extent.

We would like to thank R. Genzel, A. Harris, A. Sternberg, and H. Zinnecker for stimulating discussions and comments on the manuscript. We are grateful to A. Eckart and J. Jackson for assistance with part of the isotopic CO observations. N. J. Evans provided many valuable comments and suggestions as a referee.

APPENDIX

A GAUSSIAN CLUMP FITTING PROCEDURE

The decomposition of the observed, three-dimensional intensity distribution (main-beam brightness temperature versus two spatial coordinates and velocity) into the emission of individual, Gaussian-shaped clumps was achieved by iteratively fitting clumps to the peak position in the map, then subtracting the fitted clump and fitting the next clumps to the residual map.

Each Gaussian shaped clump was described by an intensity distribution

$$Y^{\text{fit}}(x_1, x_2, v) = a_0 \exp \left\{ -A(x_i - x_i^0, \Delta x_i, \phi) - 4 \ln 2 / \Delta v^2 [v - v^0 - \sum \alpha_i (x_i - x_i^0)]^2 \right\} + b_0,$$

where a_0 is the peak intensity of the clump, b_0 is a constant intensity offset, v^0 is the clump's center velocity, Δv is the FWHM

velocity width, α_i are the Cartesian components of the clump's internal velocity gradient vector $\partial v / \partial x_i$, and $A(x_i - x_i^0, \Delta x_i, \varphi)$ is a positive definite, two-dimensional quadratic form, characterized by the clump center position x_i^0 , the FWHM Δx_i in the two spatial coordinates, and the orientation angle φ . The spatial FWHM were expressed as $\Delta x_i^2 = \Delta_{\text{beam}}^2 + \Delta \xi_i^2$, where $\Delta \xi_i$ is the intrinsic clump FWHM size, smeared out by the limited angular resolution of the telescope (FWHM Δ_{beam}) to the observed size Δx_i . In the actual fitting procedure, the $\Delta \xi_i$ values were varied, so that the fitted clumps are forced to have an observed size at least as large as the telescope beam. This prevents the fitting procedure from trying to identify narrow noise spikes as individual clumps.

A clump with the above shape is fitted to the observed intensity map in a slightly generalized least-squares fitting procedure, where the function

$$\chi^2 = 1/n_f \sum \{w_i(Y_i - Y_i^{\text{fit}})^2 + s_0 \exp(Y_i^{\text{fit}} - Y_i)\} + s_c[\sum (x_j^0 - x_j^{\text{max}})^2/\Delta_{\text{beam}}^2 + (v^0 - v^{\text{max}})^2/\Delta_{\text{res}}^2] + s_a(a_0 + b_0 - Y^{\text{max}})^2,$$

where $Y^{\text{max}} = Y(x_1^{\text{max}}, x_2^{\text{max}}, v^{\text{max}})$ is the maximum value of the observed map, Δ_{res} is the velocity resolution, and n_f is the number of free points (number of map points minus 11), minimized by varying the 11 parameters characterizing the clump. Here $Y_i = Y(x_1^i, x_2^i, v^i)$ is the observed intensity at point i , Y_i^{fit} is the intensity at point i of the clump being fitted. All intensities are normalized to a 1σ noise level of unity in the observed map.

The first extra term (compared to a standard χ^2 fit), the one proportional to s_0 , adds a rapidly growing term to χ^2 if the fitted intensity is larger than the observed one. This way the fitted intensity distributions is kept below the observed one, which is important in order to keep the fitting routine from trying to fit two (or more) nearby local maxima by one, more extended clump. The fitted intensity in this case would have to be larger than the observed distribution in the valleys in between the local maxima.

The next extra term, the one proportional to s_c , keeps the center position of the fitted clump close to the position of the map maximum. This guarantees that the clump center cannot walk away from the initial position by much further than a resolution element, which is especially important for maxima near the map boundary, where otherwise the procedure might try to fit the observed intensity by the extended wing of a huge clump located far out of the boundaries of the observed area. The last extra term, the one proportional to s_a , keeps the peak amplitude of the fitted distribution, $a_0 + b_0$, close to the maximum value of the observed map, so that the fitting procedure is not allowed to fit a wide, less intense, underlying feature instead of a local clump at the map maximum.

In addition, the weights w_i of the observed points are chosen to decrease in a Gaussian way away from the maximum of the map, where the FWHM for the weighting function was typically chosen to be several beam widths for the spatial coordinate and 3 km s^{-1} for the velocity coordinate. It is important to realize that such a weighting function does not introduce a maximum possible clump size scale: if the observed map does only show a very wide smooth distribution, this will still be fitted properly by the least-squares procedure. The weighting function only introduces a preference to fit small-scale structure, if present, rather than the large-scale distribution of the map. For numerical convenience, only points within 2 times the FWHM of the weighting function were actually considered in the fitting procedure. Points further away do not contribute substantially anyway, because of their low weighting. This cutoff, however, drastically reduces the number of points to be treated in the calculation of χ^2 , and thus speeds up the numerical procedure substantially. The constant offset b_0 represents then, together with the tapered window introduced by the weighting function, the average intensity of other, less intense clumps nearby.

We feel that the clump fitting criteria described above are all well motivated by what one would intuitively consider a well-defined clump in a complicated intensity distribution. We tried different values of the fitting parameters s_0 , s_c , s_a , and the FWHM width of the weighting function. No large differences were found compared to the runs with the straightforward choices $s_0 = s_c = s_a = 1$ and values for the width of the weighting function given above.

Clump after clump (not the offset term b_0 , of course) was subtracted from the observed map. Occasionally, the fit would not converge, usually when the identified map maximum was close to the map boundary. This maximum point was then marked as unfittable and not considered as a starting point in further iterations. This typically occurred for about 5–10 points out of a total of about 10,000. The iteration was stopped when the integrated intensity of all subtracted clumps was equal to the original, integrated intensity of the observed map. This limit was reached after about 180 clumps, depending slightly on the settings of the fitting parameters. The peak intensity of the residual map was then typically a few times the 1σ noise level.

The clump fitting was done on the observed data cube binned to 0.50 km s^{-1} velocity resolution. For the fitting procedure, the appropriately modified least-squares fit routine CURFIT (Bevington 1969) was used. The partial derivatives of the fit function with respect to all 11 parameters to be fitted were evaluated analytically. Each individual clump fitting process was considered to have converged when the parameters did not change anymore by more than 1% in three successive iterations. This took typically between 5–50 iterations. The total decomposition procedure (180 clumps) required about 3 hr CPU time on a $\mu\text{VAX 3500}$ station.

We tested the clump fitting procedure with a set of synthesized data. A clumpy cloud was simulated with a Monte-Carlo procedure creating an ensemble of clumps with a specified mass spectrum. The power-law index of the mass spectrum, which was varied between $M^{-1.1}$ and $M^{-1.75}$ in the simulations, was recovered in the Gaussian decomposition procedure to within a value of 0.1. For simulated clouds with very densely packed core regions, the decomposition procedure has the tendency to slightly underestimate the index of the actual spectrum. This results from the confusion in identifying individual clumps in the inner region. The identification of an unresolved ensemble of lower mass clumps as one bigger clump flattens out the power-law spectrum. However, this seems not to affect the mass spectrum for the number density of clumps found in the M17 SW cloud core.

The size, line width, and intensity distribution of the fitted clumps matched the original distribution quite well. In particular, the clump fitting procedure does not introduce a preferred length scale or velocity width for the clumps. To test the effects of non-Gaussian clump shapes on the resulting mass spectrum, a set of circular clumps with constant surface brightness was investigated. The resulting fitted mass spectrum still represents the original mass spectrum of the synthesized clumps. However, as expected, the procedure fits a number of additional, small clumps around the perimeter of the original clumps, which show up as a tail of low-mass clumps in the resulting spectrum.

REFERENCES

- Arny, T., and Weissman, P. 1973, *A.J.*, **78**, 309.
- Bevington, P. R. 1969, *Data Reduction and Error Analysis for the Physical Sciences* (New York: McGraw-Hill).
- Bieging, J. H., Wilson, T. L., and Downes, D. 1982, *Astr. Ap. Suppl.*, **49**, 607.
- Blake, G. A., Sutton, E. C., Masson, C. R., and Phillips, T. G. 1987, *Ap. J.*, **315**, 621.
- Blitz, L. 1987, in *Physical Processes in Interstellar Clouds*, ed. G. E. Morfill and M. Scholer (Dordrecht: Reidel), p. 35.
- Blitz, L., and Stark, A. A. 1986, *Ap. J. (Letters)*, **300**, L89.
- Boissé, P. 1989, preprint.
- Casoli, F., Combes, F., and Gérin, M. 1984, *Astr. Ap.*, **113**, 99.
- Chini, R., Elsässer, H., and Neckel, Th. 1980, *Astr. Ap.*, **91**, 186.
- Dickey, J. M., and Garwood, R. W. 1989, *Ap. J.*, **341**, 201.
- Evans, N. J., Kutner, M. L., and Mundy, L. G. 1987, *Ap. J.*, **323**, 145.
- Evans, N. J., Mundy, L. G., Davis, J. H., and Vanden Bout, P. 1987, *Ap. J.*, **312**, 344.
- Falgarone, E., and Péroult, M. 1987, in *Physical Processes in Interstellar Clouds*, ed. G. E. Morfill and M. Scholer (Dordrecht: Reidel), p. 59.
- Felli, M., Churchwell, E., and Massi, M. 1984, *Astr. Ap.*, **136**, 53.
- Field, G. B., and Hutchins, J. 1968, *Ap. J.*, **153**, 737.
- Field, G. B., and Saslaw, W. C. 1965, *Ap. J.*, **142**, 568.
- Gatley, I. R., Becklin, E. E., Sellgren, K., and Werner, M. W. 1979, *Ap. J.*, **233**, 575.
- Genzel, R., Harris, A. I., Jaffe, D. T., and Stutzki, J. 1988, *Ap. J.*, **332**, 1049.
- Genzel, R., et al. 1990, in preparation.
- Güsten, R., and Fiebig, D. 1988, *Astr. Ap.*, **204**, 253.
- Harper, D. A., Low, F. J., Rieke, G. H., and Thronson, H. A. 1976, *Ap. J.*, **205**, 136.
- Harris, A. K. 1988, *Internat. J. Infrared Millimeter Waves*, **9**, 231.
- Harris, A. I., Stutzki, J., Genzel, R., Lugten, J. B., Stacey, G. J., and Jaffe, D. T. 1987, *Ap. J. (Letters)*, **322**, L49.
- Ho, P. T. P., and Townes, C. H. 1983, *Ann. Rev. Astr. Ap.*, **21**, 239.
- Icke, V., Gatley, I. R., and Israel, F. 1980, *Ap. J.*, **235**, 808.
- Jaffe, D. T., Güsten, R., and Downes, D. 1981, *Ap. J.*, **250**, 621.
- Keene, J., Blake, G. A., Phillips, T. G., Huggins, P. J., and Beichman, C. A. 1985, *Ap. J.*, **299**, 967.
- Kleinmann, D. E., and Wright, E. L. 1973, *Ap. J. (Letters)*, **185**, L131.
- Kutner, M. L., and Ulich, B. L. 1981, *Ap. J.*, **250**, 341.
- Lada, C. J., Dickinson, D. F., Gottlieb, C. A., and Wright, E. L. 1976, *Ap. J.*, **207**, 113.
- Larson, R. B. 1981, *M.N.R.A.S.*, **194**, 809.
- Lizano, S., and Shu, F. H. 1989, *Ap. J.*, **342**, 834.
- Loren, R. B. 1989a, *Ap. J.*, **338**, 902.
- . 1989b, *Ap. J.*, **338**, 925.
- Lovas, F. J., and Krupenie, P. H. 1974, *J. Phys. Chem. Ref. Data* **3**, 245.
- Martin, H. M., Sanders, D. B., and Hills, R. E. 1984, *M.N.R.A.S.*, **208**, 35.
- Massi, M., Churchwell, E., and Felli, M. 1988, *Astr. Ap.*, **194**, 116.
- Matsakis, D. N., Brandshaft, D., Chui, M. F., Cheung, A. C., Yngvesson, K. S., Cardiasmenos, A. G., Shanely, J. F., and Ho, P. T. P. 1977, *Ap. J. (Letters)*, **214**, L67.
- Moore, T. J. T., Chandler, C. J., Gear, W. K., and Mountain, C. M. 1989, *M.N.R.A.S.*, **237**, 1p.
- Mundy, L. G., Evans, N. J., Snell, R. L., and Goldsmith, P. F. 1987, *Ap. J.*, **318**, 392.
- Mundy, L. G., Snell, R. L., Evans, N. J., Goldsmith, P. F., and Bally, J. 1986, *Ap. J.*, **306**, 670.
- Nakano, T. 1984, *Fund. Phys.*, **9**, 139.
- Penzias, A. A. 1981, *Ap. J.*, **249**, 518.
- Péroult, M., Falgarone, E., and Puget, J. L. 1985, *Astr. Ap.*, **152**, 371.
- Perry, J. F., and Helfer, H. L. 1972, *Ap. J.*, **174**, 341.
- Rainey, R., et al. 1987, *Astr. Ap.*, **171**, 252.
- Sanders, D. B., Scoville, N. Z., and Solomon, P. M. 1985, *Ap. J.*, **289**, 373.
- Scalo, J. M. 1985, in *Protostars and Planets II*, ed. D. C. Black and M. Shapley Mathews (Tucson: University of Arizona Press), p. 201.
- Schulz, A., Gillespie, A. R., and Krügel, E. 1985, *Astr. Ap.*, **142**, 363.
- Silk, J., and Takahashi, T. 1979, *Ap. J.*, **229**, 242.
- Snell, R. L., Goldsmith, P. F., Ulich, B. L., Lada, C. J., Martin, R., and Schulz, A. 1986, *Ap. J.*, **304**, 780.
- Snell, R. L., Mundy, L. G., Goldsmith, P. F., Evans, N. J., and Erickson, N. R. 1984, *Ap. J.*, **276**, 625.
- Spitzer, L. 1982, *Searching between the Stars* (New Haven: Yale University Press), pp. 148–151.
- Stacey, G. J., Geis, N., Genzel, R., Harris, A. I., Jaffe, D. T., Poglitsch, A., and Stutzki, J. 1989, *Bull. AAS*, **21**, 4.
- Stutzki, J., Genzel, R., and Harris, A. I. 1990, in preparation.
- Stutzki, J., Jackson, J. M., Olberg, M., Barrett, A. H., and Winnewisser, G. 1984, *Astr. Ap.*, **139**, 258.
- Stutzki, J., Stacey, G. J., Genzel, R., Harris, A. I., Jaffe, D. T., and Lugten, J. B. 1988, *Ap. J.*, **332**, 379.
- Stutzki, J., and Winnewisser, G. 1985, *Astr. Ap.*, **144**, 13.
- Taff, L. G., and Savedoff, M. P. 1972, *M.N.R.A.S.*, **160**, 89.
- . 1973, *M.N.R.A.S.*, **164**, 357.
- Thronson, H. A., and Lada, C. J. 1983, *Ap. J.*, **269**, 175.
- Tutukov, A. W., and Shustov, B. M. 1981, *Astr. Zh.*, **58**, 109.
- Wilson, T. L., Serabyn, E., Henkel, C., and Walmsley, C. M. 1986, *Astr. Ap.*, **158**, L1.
- Yorke, H. W. 1979, *Astr. Ap.*, **80**, 308.
- Zinnecker, H. 1989, in *Evolutionary Phenomena in Galaxies*, ed. J. Beckman (Cambridge: Cambridge University Press), p. 115.

R. GÜSTEN: Max-Planck-Institut für Radioastronomie, Auf dem Hügel 69, D-5300 Bonn 1, Federal Republic of Germany

J. STUTZKI: Max-Planck-Institut für Physik und Astrophysik, Institut für Extraterrestrische Physik, D-8046 Garching bei München, Federal Republic of Germany